A Novel Ground Based Mass-Balance Method for Methane Emission Quantification

William Fujs

A Thesis Submission to

The Faculty of Graduate Studies

In Partial Fulfillment of the Requirements For the Degree of Master of Science

Graduate Program in

Chemistry

York University

Toronto, Ontario

April 2018

Abstract

Emission of CH_4 from landfills in Canada are not well constrained and in Ontario constitute the largest point source emitters. The purpose of this study was to develop and test a ground based method for quantifying CH_4 emissions from large sources. Emissions of CH_4 were quantified from the Keele Valley Landfill (KVL) using ground based mobile mass balance approach where a mobile cavity ring down spectroscopy (CRDS) instrument captured the downwind field of CH_4 mixing ratio enhancements relative to the background. The approach involves measuring the downwind field of enhancements at successively further distances from the source until the integrated CH_4 enhancements converge. On multiple days in April and May 2016 multiple transects were driven upwind and at increasing distances downwind from the KVL with the CRDS in a vehicle in order to determine integral flux emission estimates. The KVL was found to be a major local source of CH_4 even though CH_4 collection used for electricity generation is now terminated. An average emission rate of 429 ± 199 kg/hr of CH_4 was measured in 2017 on several days, which is less than the ECCC emission inventory value of 2149 kg/hr [2015]. The source of the discrepancy is not fully understood, but may be related to the shutdown of the KVL facility. The largest source of uncertainty in our emission estimate calculation was the height of the PBL, which was estimated using publically available AMDAR take-off and landing data at airports in southern Ontario and northern New York State. A locally measured PBL height would reduce the uncertainty of the emission estimate. A long path Tunable Diode Laser Spectroscopy Instrument was also deployed tested in this study but its maximum path length was found not to be sufficient to capture the KVL source. This study demonstrates the feasibility of this low cost, high spatial and temporal resolution method for estimating top-down CH_4 emissions from ground level sources. This method could be used to validate relatively unrestrained bottom-up emission inventories, which can improve radiative forcing CH_4 modelling.

Acknowledgements

I would first like to thank my supervisor Dr. Robert McLaren for his unending support and guidance through the process of completing both this project and thesis. His supervision challenged me when needed and helped me grow as a future scientist and professional. I would also like to thank my committee members Dr. Jochen Rudolph and Dr. Shao-Meng Li for their suggestions and hard questions.

I would also like to thank the members of the research group who played integral roles in the preparation and completion of the field study including Aida, Zoe, Sabour and Csilla. I would like to thank ECCC for lending us the Piccaro, which allowed this project to move forward. Finally I would like to thank the NSERC Create program IACPES and York University's Faculty of Graduate Studies for the funding I received that enabled this project to take place.

TABLE OF CONTENTS

List of Tables

List of Figures

1.0 Introduction

1.1 Methane

Methane (CH_4) is an important atmospheric trace gas that is well known to play a major role in climate, by acting as a Greenhouse Gas (GHG). Although considered unreactive in the atmosphere, it can play a role in O_3 formation and may also play a role in air quality when emitted at higher concentrations. Current global background levels of CH_4 (concentrations in unpolluted areas away from sources), are roughly 1850 ppb (Dlugokencky, 2017). This mixing ratio is more than double what was present before the Industrial Revolution in the mid-1800's. Ice core samples have shown that pre-industrial values of CH_4 have ranged from 350 ppb, during glacial time periods, to 700 ppb, during interglacial times (Chappellaz et al, 1993). During these pre-industrial times the major source of CH_4 in the atmosphere was natural wetlands which produced CH_4 through the anaerobic decomposition of organic material. Nearly all methane is produced through a similar process which begins with the fermentation of organic material to acetic acid (CH_3COOH). This acid is then converted to CH_4 by methanogenic Archaea (Conrad, 1996). Annual precipitation and temperature were the major factors that governed CH_4 production from these wetlands and therefore, the global budget of CH_4, higher temperatures and precipitation were linked to higher CH_4 emissions (Fung et al, 1991). Up to 70% of CH_4 emissions at that time were from lower latitudes and can act as a guide to historical climate trends. Seasonal trends follow the same pattern with warmer months seeing an increase in CH_4 emissions.

Since the industrial revolution GHG's atmospheric concentrations have been on the rise (Figure 1). CH_4 levels rose consistently until the late 1990's when they reached a plateau of nearly 1750 ppb (Dlugokencky, 1992). This levelling-off of CH_4 levels was first attributed to an 8 Tg decrease in fossil fuel production during the early 1990's. It was hypothesized that the destabilization of the Soviet Union at the beginning of the 1990's reduced emissions from fossil fuel production facilities. It was reported that

CH_4 levels were once again on the rise starting in 2007 after being constant for nearly a decade (Rigby, 2008). It was shown that the OH radical, the major sink of CH_4 in the atmosphere, had remained constant while increased emissions of CH_4 from both hemispheres were being observed, although this has recently been questioned (Turner et al., 2017).

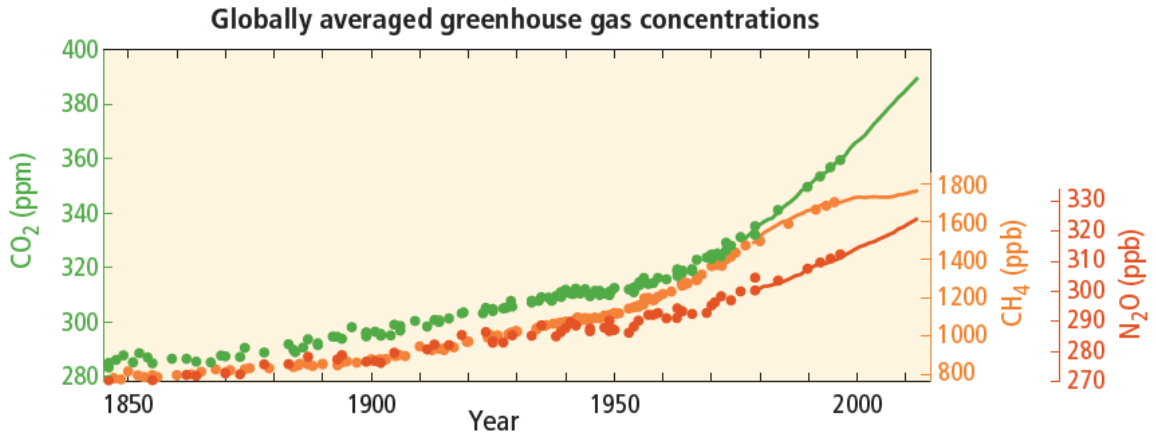

Figure 1: Historical GHG levels on the rise since the Industrial Revolution. Showing CO_2, CH_4 and N_2O from IPCC AR5 2014.

More recent work has shown ambiguity in global OH levels as well as emissions of CH_4. One recent study looked at 1,1,1-trichloroethane (CH_3CCl_3) to infer decreasing OH levels (Rigby et al, 2016). This was justified due to CH_3CCl_3's major loss mechanism being a reaction with OH. The modelling study here showed with 64-70% probability that a decline in OH contributed to the rise in global CH_4. This study also showed a rise in $^{13}CH_4/^{12}CH_4$ and ethane (C_2H_6), another tracer for increased oil and gas extraction.

Recent work has begun emphasizing the importance a decrease in OH would have on global levels of CH_4. One of these recent modelling studies argued that the renewed increase in CH_4 levels could have arisen as a result of the decrease in CH_4 emissions by 25 Tg/yr which were being offset by a decrease in global OH by 7%. Since OH is the major sink of CH_4 in the atmosphere it was shown that a decrease in OH would have a stronger impact than a decrease in CH_4 emissions (Turner et al 2017). Through a

rigorous modelling exercise, aided by ground based measurements of $\delta^{13}CH_4$ and methyl chloroform, it was shown that this decrease could be a cause for the recent increase in CH_4 in both hemispheres. This paper also details how their model explains the plateau in CH_4 concentration from 1993 to 2003 coming as a result of a 35 Tg/yr increase CH_4 emissions coinciding with a 7% increase in OH levels. These increases offset one another and kept the observed CH_4 levels constant globally at this time.

There are two categories that emission estimates can be grouped into; top-down and bottom-up. Top-down measurements are generally "real world" measurements of the total emissions from large sources where it is often difficult to distinguish between individual sources (Petron et al, 2014). Bottom-up emission estimates present in emission inventories for example, result from calculations using emission factors combined with activity data that can be aggregated to estimate total emissions from a source, which may miss emissions and not be representative of an overall source. The most robust emission estimates may combine both top-down and bottom-up approaches in order to more accurately characterize the emission sources in a given area (Rella et al 2015). In addition to understanding where emissions come from, their relative impact on the atmosphere is also important.

One of the most important climatically relevant characteristics of an individual gas species is its radiative forcing (RF). RF is the change in the Earth's radiation budget, the balance of shortwave radiation absorbed from the sun and emitted by the Earth's surface caused by the change in concentration of a specific species ($W\ m^{-2}$) (See Figure 2).

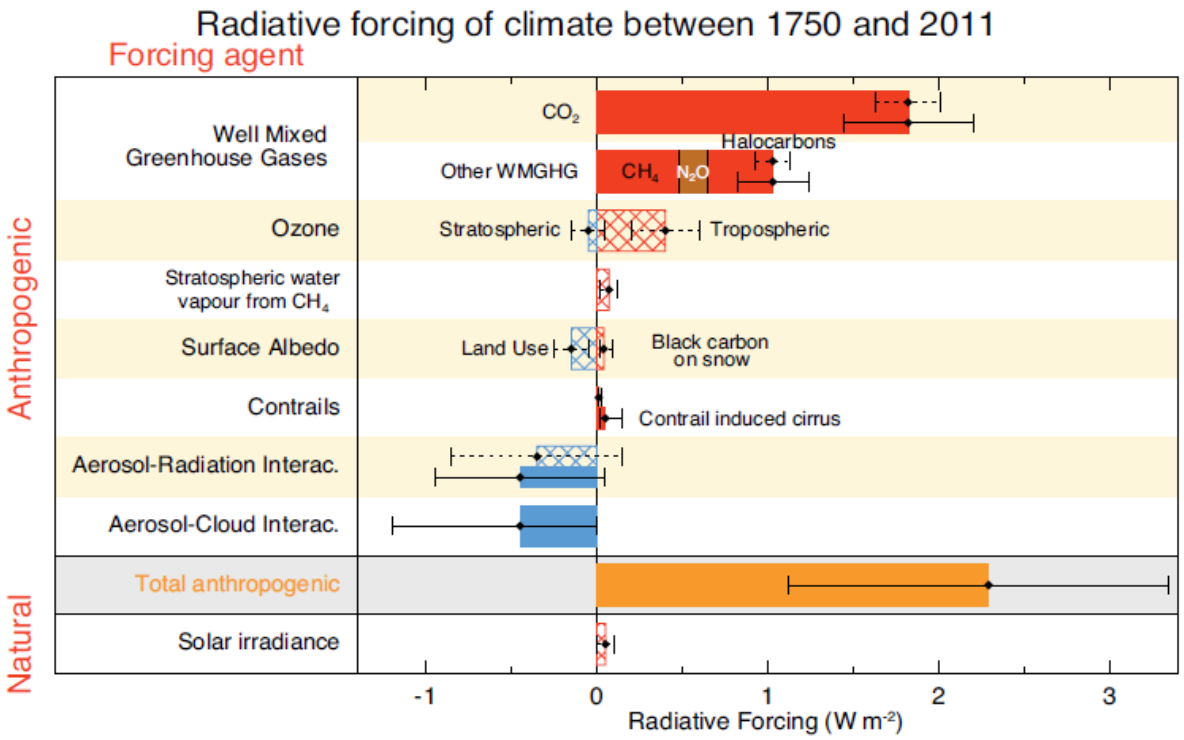

Figure 2; Radiative forcing of major GHG's, including CH_4, from the IPCC AR5 Chapter 8, Anthropogenic and Natural Radiative Forcing, 2014

Species which cause an increase in net downward radiation within the atmosphere has a positive RF resulting in warming. Gases that decrease Earth's radiation flux have a negative RF and cause cooling. Some species, like O_3, are capable of having a positive RF in the troposphere and a negative RF in the stratosphere where wavelengths of light below 336 nm are absorbed by O_3 before reaching the ground (Crutzen, 1993). One way in which gas species are compared is through their Global Warming Potential (GWP). GWP's are a measure of the change in the radiative forcing caused by a release of 1 ton of a gas relative to 1 ton of CO_2 (IPCC AR5, 2014). The GWP of CH_4 is roughly 28 higher than CO_2 over 100 years. This is due to CH_4 absorbing much more radiation energy than CO_2 despite having much shorter lifetime in the atmosphere.

The underlying principle of a GWP is closely related to the ability of a gas to act as a greenhouse gas. Incoming shortwave radiation from the sun is absorbed by the Earth's surface. The surface re-emits this

energy as long wavelength radiation mostly in the infrared portion of the spectrum (4 – 100 µm) back into the atmosphere to maintain a radiative balance. Some of this radiated energy will be absorbed by greenhouse gases where it can be either emitted into space, acting to cool the atmosphere, or back down to the ground where it provides extra warming giving rise to the term Green House Gases (GHGs). Part of CH_4's importance lies in its absorption at 3312.26nm and 7692.31nm which is a region where no other atmospheric species absorb a significant portion of the light spectrum and a region where light can be radiated back out into space (Figure 3). As CH_4 levels rise, more of this light energy is absorbed in the atmosphere and a portion is radiated back towards earth.

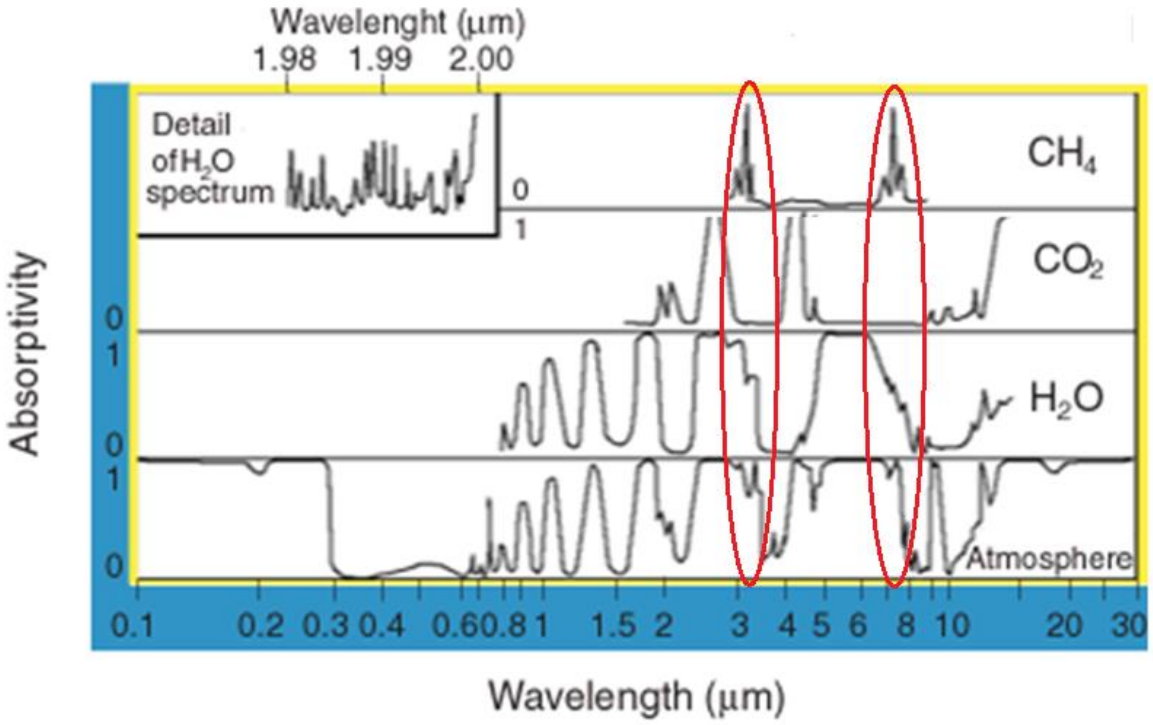

Figure 3; Modified from Fleagle and Businger 1963 depicting the unique absorption lines by CH_4 in the Earth's atmosphere as they relate to trapping IR light.

In order to understand the impact that CH_4 has at the ground level the stratification of the atmosphere must first be discussed. The atmosphere is meteorologically separated into different regions based on

temperature gradients with respect to height. The region closest to the ground is called the troposphere in which the temperature decreases with height at a rate of ~ 6.5 K/km (Warneck, 1988). The troposphere reaches a height of roughly 12-20 km, wherein the temperature decrease slows and becomes constant in the top 2-3 kilometres, a region called the tropopause. Above the tropopause is the stratosphere, a region which has increasing temperature with height. Above the stratosphere is the mesosphere where temperatures again decrease to a minimum of 185 K. The outermost region of the atmosphere is called the thermosphere where temperatures once again rise with height. Temperature is a measure of average kinetic energy of the air molecules, which is on average a constant balance between the energy absorbed from the sun and light reflected back into space (at wavelengths greater than 3 μm).

Only a small portion of solar radiation is absorbed by optically active species while the majority reaches the earth's surface. This surface heating causes local convection transferring heat into the air which expands as it rises. As the air expands it cools causing the troposphere's temperature gradient. The lowest portion of the troposphere is called the Planetary Boundary Layer (PBL) which is directly affected by this convection as well as frictional drag of the atmosphere over the uneven surface of Earth. The height of the PBL varies diurnally stretching to a height of 0.5-2km during the day, and shrinks to as low as 100 m during the night. Emissions made at the ground level will take time before they are able to mix vertically to the full height of the PBL.

The lifetime of CH_4, or the average time it is expected for one molecule of CH_4 to remain in the atmosphere until it is removed through either a chemical reaction or physical process, is ~ 9 years. This is a relatively short amount of time when compared with other trace gas species like CO_2, which has a lifetime of nearly 120 years (IPCC, 2001). This makes CH_4 an ideal target for reduction in emissions as its impact would be felt in the more immediate future.

Methane is the most abundant organic gas species found in the atmosphere. The largest sink of methane is its oxidation initiated by the OH radical through a multi-step process that ends with the production of formaldehyde (Crutzen 1993).

$$CH_4 + OH \rightarrow CH_3 + H_2O \quad (1)$$

$$CH_3 + O_2 + M \rightarrow CH_3O_2 + M \quad (2)$$

$$CH_3O_2 + NO \rightarrow CH_3O + NO_2 \quad (3)$$

$$CH_3O + O_2 \rightarrow HCHO + HO_2 \quad (4)$$

These reactions have an indirect role on the odd hydrogen budget, which includes H, OH and HO_2. These species are grouped together due to their rapid interconversion amongst themselves and their common process of destroying stratospheric O_3. The formaldehyde that is produced in the last step of CH_4 oxidation (Equation 4) is then able to undergo its own series of oxidation steps to produce CO_2.

$$HCHO + O_2 \rightarrow CO + O_3 + H_2O \quad (5)$$

$$CH_2O + h\upsilon \rightarrow CO + 2H \quad (6)$$

$$CO + 2O_2 \rightarrow CO_2 + O_3 \quad (7)$$

The net product for the oxidation of CH_4 includes O_3, which can cause poor air quality and lead to adverse health effects in the lowest 2 km of the atmosphere.

The major source of OH in a remote area of the atmosphere is the photolysis of O_3 that produces an electronically excited $O(^1D)$ and O_2 molecule. This excited atom can either react with H_2O to produce OH or relax to $O(^3P)$ through the following processes.

$$O_3 + h\upsilon\ (\upsilon < 336\ nm) \rightarrow O(\ ^1D) + O_2 \quad (8)$$

$$O(\ ^1D) + H_2O \rightarrow 2OH \quad (9)$$

$$O(\ ^1D) + M \rightarrow O(\ ^3P) \quad (10)$$

A secondary formation pathway for O(^{1}D) exists and is less common at higher altitudes as there is less H_2O present to initiate that reaction. In polluted areas, nitrous oxide (HONO), hydrogen peroxide (H_2O_2) and HO_2 in the presence of NO can all be seen as sources of OH radical as well.

$$HONO + h\upsilon\ (\upsilon < 336\ nm) \rightarrow OH + NO\cdot \quad (11)$$

$$H_2O_2 + \ h\upsilon\ (\upsilon < 336\ nm) \rightarrow OH \quad (12)$$

$$HO_2 + NO \rightarrow OH + NO_2\cdot \quad (13)$$

These reactions are photolytic and cause OH to be the major atmospheric oxidant during the daytime while other minor sources of OH from the oxidation of alkenes by O_3 exist.

The International Panel on Climate Change (IPCC), the branch of the United Nations (UN) which evaluates climate science and was founded in 1988, releases large scale reports on GHG emissions and trends. The IPCC's most current published material is from 2014 and is its fifth Assessment Report (IPCC AR5, 2014). This document outlines the source and sinks of all GHG's along with historical trends and outlines possible future outcomes based on current and projected global emissions. AR5 states that anthropogenic, or man-made, emissions are the cause for the recent rise in GHG concentrations. These emissions were shown to cause a rise in mean surface temperature and it is projected that this rise will continue to grow with continued growth in emission rates (Figure 4).

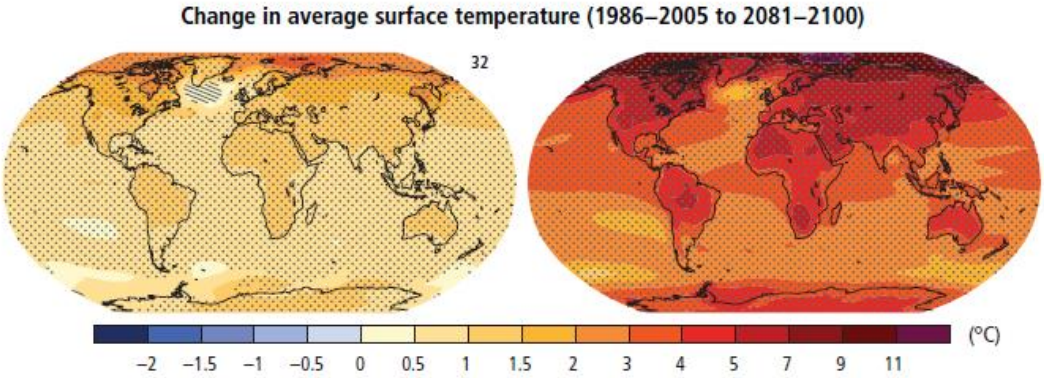

Figure 4; The current and projected change in surface temperature from IPCC AR5, 2014

Global emissions of GHG's reached 49 ± 4.5 $GtCO_2$-eq/yr, based on 100-year GWP in 2010. AR5 reported that CH_4 makes up 16% (or 7.84 $GtCO_2$-eq/yr) of these overall emissions. The major driver for increased emissions was shown to be economic and population growth. Anthropogenic sources of GHG are grouped into electricity production (25%), agriculture (24%), industry (21%), transport (14%), buildings (6.5%) and other (9.6%).

Canada follows the guidelines presented by the IPCC and presents their GHG inventories in the following categories; energy, agriculture, waste and industrial processes. The highest emitted GHG in Canada (measured in 100 year CO_2 GHG equivalents) is CO_2 at 79% followed by CH_4 at 14%, N_2O at 5% and HFCs, PFCs and SF_6 making up the remaining 1.7% (Fig. 5).

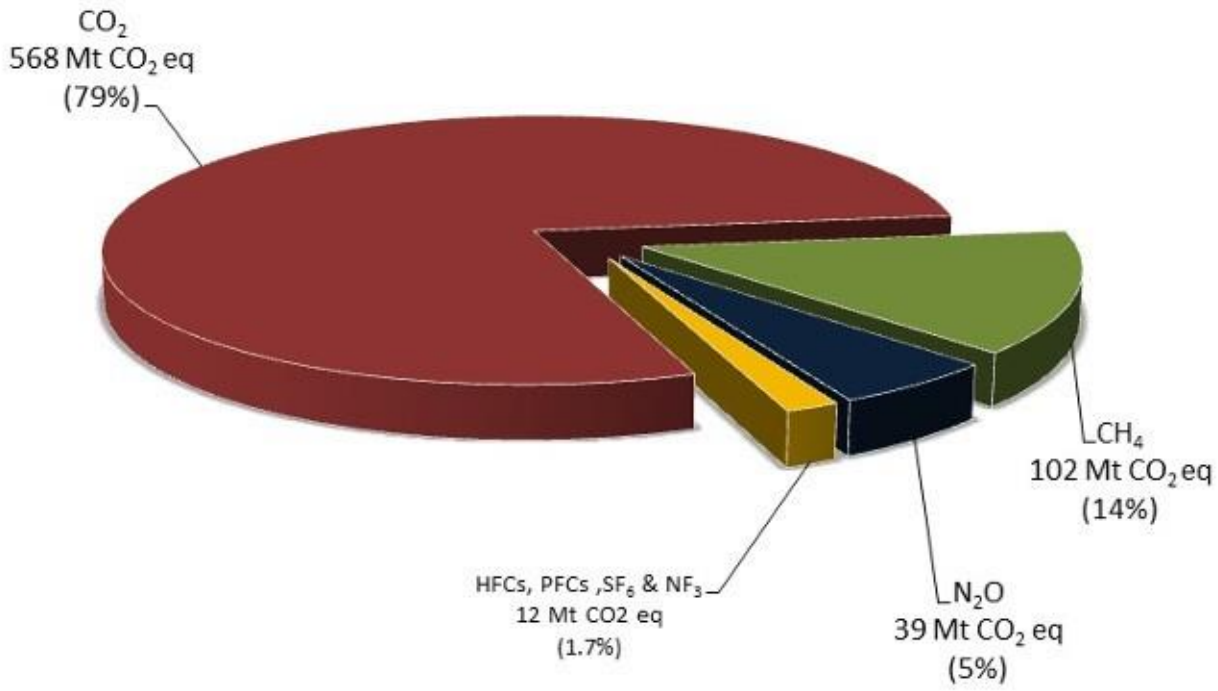

Figure 5; Canada's GHG emission by gas in 2015 as reported by Environment and Climate Change Canada totalling 721 Mt CO2 eq. (figure retrieved from; https://www.canada.ca/en/environment-climate-change/services/climate-change/greenhouse-gas-emissions/seventh-national-communication-third-biennial-report.html)

Due to emissions from the energy sector being so large it is broken down into three subcategories; stationary combustion, transport and fugitive sources. These emissions are largely due to combustion of fossil fuels producing CO_2, H_2O and mechanical heat or energy. Stationary combustion sources include power plants, the oil and gas industry and residential and commercial sectors. Transportation includes road, railway, aviation, off-road vehicles and domestic marine. Fugitive emissions include intentional flaring and accidental leaks of GHG into the atmosphere from production, transportation and storage of fuel and landfills.

1.2 Methane from Landfills

Waste production has been shown to be closely tied to a country's gross domestic product (GDP) and energy consumption. Current global rates of solid waste production are in the range of 900-1300 million tonnes per year (IPCC, 2016). Global GHG emissions from landfills have continually risen from 6% in 1970 to 9% in 2008, of overall emission sources (Figure 6). Methane production in landfills is generated from the decomposition of organic material in an anaerobic environment. Nearly all CH_4 is produced through a process of converting fermented acids, which are the by-products of anaerobic decomposition, to CH_4 by methanogenic Archaea (Conrad, 1996).

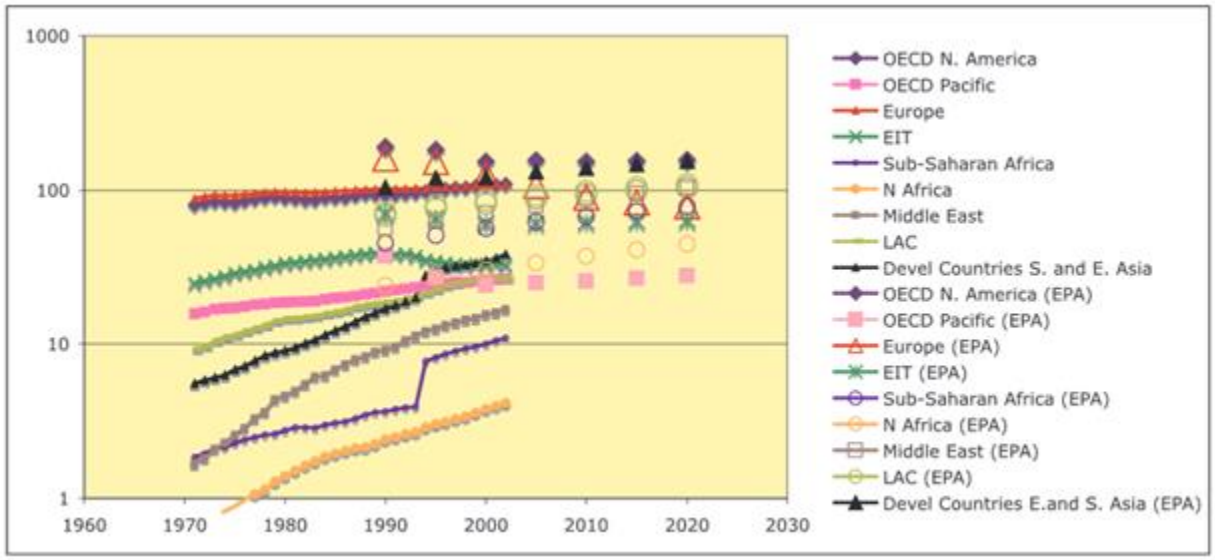

Figure 6; GHG Emission trends from Landfill sources reported in Mt CO2-eq, from Bogner et al 2008

Emissions of CH_4 over this time rose from 734 M tonnes to 1400 M tonnes from landfill and waste facilities (Bogner, 2008). The trend of emission growth has slowed in recent years as GHG recovery and utilization for energy production has become more widespread. As of 2003 there were 1150 landfill

plants worldwide actively recovering GHG's resulting in an estimated reduction in emissions by 105 Mt CO_2-eq $year^{-1}$. This value was shown to be an expected minimum as many sites, predominantly in developing countries, collect the GHG's but then flare the CH_4. Previous direct small-scale measurements of landfill emissions have shown emission rates to range from 0.0001 g to over 1000 g CH_4 m^{-2} per day (Bogner et al 1997).

The IPCC outlines two methods to estimate GHG emissions from landfills; the default method and the First Order Decay (FOD) method. The default method is based on work by Bingemer and Crutzen (1987) and has CH_4 emissions, in T/yr, being the product of MSW_T, total municipal solid waste, MSW_F, fraction of solid waste disposed at the site, MCF, a methane correction factor, DOC, the fraction of degradable organic carbon, and DOC_F, the fraction of DOC dissimilated;

$$Methane\ Emission = (MSW_T \times MSW_F) \times MCF \times DOC \times DOC_F \times F \times \left(\frac{16}{12} - R\right) \times (1 - O_x R) \quad (14)$$

Where F is the fraction of CH_4 in the landfill gases, R is the amount of recovered methane and O_X is the oxidation factor to account for CH_4 that is oxidized in the soil where O_2 is present before escaping into the atmosphere. The FOD method follows a triangular approach where CH_4 emissions are assumed to first rise and then degrade over time (see Figure 7). The CH_4 emitted at a given time after the initial closure of a landfill is calculated as the area of the triangle underneath the peak.

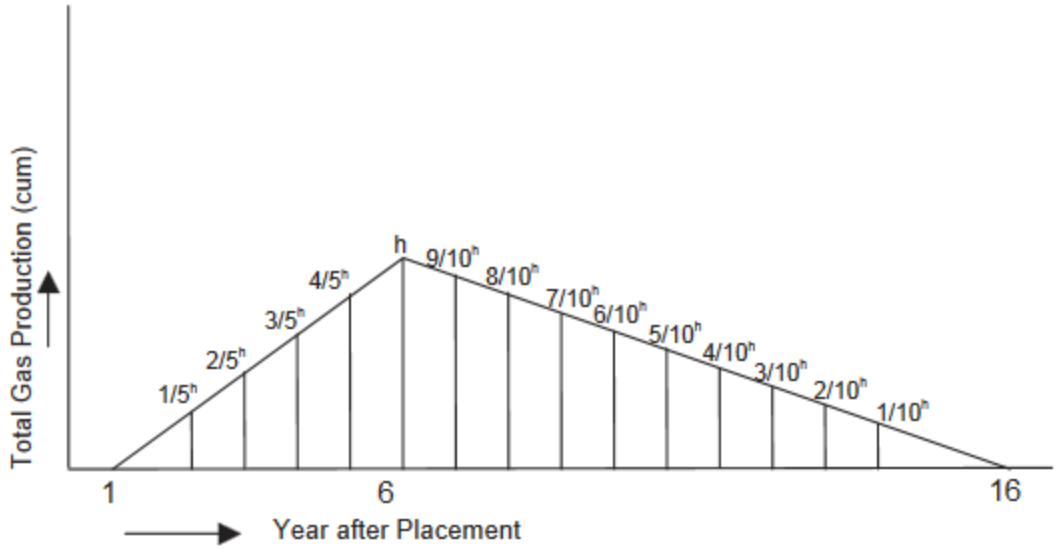

Figure 7; Triangular form of gas production in a landfill following the FOD method outlined by the IPCC (IPPC, 2016)

The Keele Valley Landfill (KVL) is located in Vaughan, Ontario, Canada, nearly 30km north of Toronto which operated from 1983 until 2002 and is the third largest landfill in North America. It was designed to hold 33,000,000 m^3 of solid waste and had a maximum depth of 65m and is covered by 1m of soil (Flemming, 1999). During its construction and during its operation a number of instruments were installed to measure water levels, temperature and gas collection. The gas collection system consists of over 40000m of underground pipes which collect emitted gas directed to an electric power plant which consists of a boiler and flaring unit. Only 5% of the collected gas is flared, to ensure no backups in the system, while the rest is cleaned from impurities and moisture and used in the boiler. At optimal performance the steam powered turbine produced 33 MegaWatts continuously. The power plant was closed in 2016 and we have been told that the CH_4 is still collected but now flared.

The KVL emission inventory reports that 20,669 tonnes of CH_4 is released each year (Reported Facility Greenhouse Gas Data, Environment Canada Inventory, 2015). This makes the site the second largest single point source of CH_4 in the province of Ontario behind only Ridge Landfill, in Blenheim ON, at 21,516 tonnes and larger than the natural gas distribution infrastructure, at 12,684 tonnes of CH_4. The emissions inventory for the KVL was carried out by Stantec, an accredited environmental consultant company, who have not published their methods of quantification for this site. Previous studies of the KVL have focused on monitoring leachate, the water that filters through the waste of a landfill, for contaminants and oxygen demand (Fleming, Rowe and Cullimore, 1999). This was done by analyzing the precipitation of $CaCO_3$ which precipitates as a by-product of organic acids being anaerobically digested increasing the pH of the leachate.

1.3 Instrumental Methods for Measuring CH_4

Early quantification of CH_4 was carried out through Gas Chromatography (GC). This is a method based on the separation of gases moving through a narrow column with an analyte dissolved in a carrier gas, often He, N_2 or H_2 (Harris, 2007). The earliest GC measurements took place in the 1950's using a technique similar to that of today where separation of gases take place within a heated column which is coated with a non-volatile liquid (Doering, 1956). CH_4 is commonly measured using a Flame Ionization Detector (FID) or a Thermal Conductivity Detector (TCD) as they are both sensitive to organic compounds (Hedley et al, 2006). CH_4 can be collected on-line with the instrument being deployed at a target site or gases can be collected with canisters/bags and brought back to the GC to be analyzed at a later date (Heeman et al, 2014).

The Tunable Diode Laser Absorption Spectroscopy (TDLAS) is an absorption based technique which uses a semiconductor to produce a light source in the near-IR region (Lackner, 2007). The earliest work producing a lasing effect was carried out using lead-based salts emitting light at 6.6 µm (Butler et al,

1964). The general experimental setup has remained the same with a diode light source directed towards a detector with the analyte in between these two. The wavelength emitted by the diode can be tuned by either altering the temperature or current applied to the laser. Gas concentrations are then calculated through the Beer-Lambert law (Shemshad, Aminossadati and Kizil, 2012).

$$T_v = (\frac{I(v)}{I_o(v)})_v = e^{-\sigma(v)xL} = e^{-\alpha(v)} \quad (15)$$

where α(v) is the transmission coefficient, I and I_o are the incident and transmitted light at a given frequency. The target gas's cross section, σ(v), is used in combination with the path length, L, to determine the analyte concentration, x. Early measurements of CH_4 with TDLs was carried out with a He-Ne laser at 3.392 µm (Moore, 1965). Open air CH_4 monitoring took place in 1985 in a wooded area using a portable Pb-salt based diode (Koga, Kosaka and Sano, 1985). The requirement for more portable Tunable Diode Laser (TDL) instrumentation resulted in the majority of systems to move to using Gallium based lasers as they can detect CH_4 at wavelengths lower than 2 µm (Mohebati and King ,1988).

The Cavity Ring-Down Spectroscopy (CRDS) is a highly sensitive absorption technique relying on the absorption of a monochromatic light source by a target gas analyte. The earliest suggestion of using an internal cavity to measure the 'ring down' of a molecule took place in 1980 (Herbelin, 1980). The underlying principle involved turning on and off a light source inside of a closed cavity, containing the trace gas to be measured, and measuring the rate of decay of light. The first detection of loss of light being reflected from optical mirrors was demonstrated in 1984 enabling the CRDS system to be fully understood (Anderson, Frisch and Masser, 1984). Current CRDS systems rely on this same principle where a near-infrared light source is transmitted into a cavity where it is reflected off either two or three mirrors which have close to 100% reflectivity. The light source is abruptly stopped and the light intensity within the cavity decays in an exponential fashion. The decay of light leaked through the mirror and seen by the detector is referred to as the "ring down" and measured by a photodetector (Figure 8).

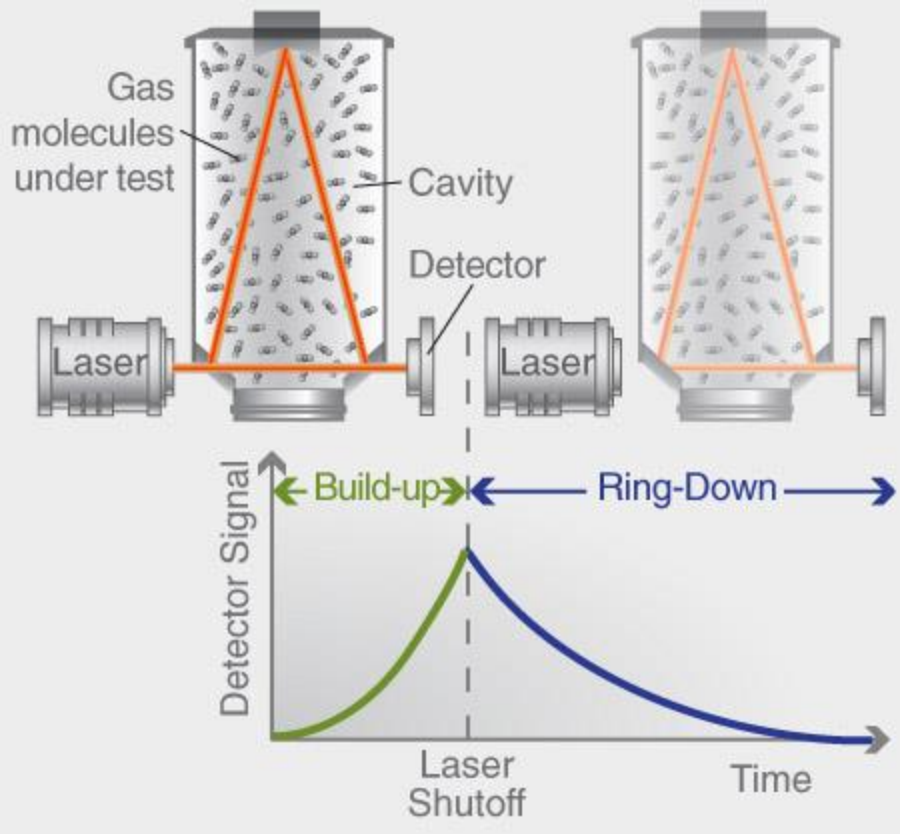

Figure 8; Depiction of the inner workings of a Cavity Ring Down Spectrometer. Image from; http://www.picarro.com/technology/cavity_ring_down_spectroscopy

When a gas species, that absorbs light at the diode transmitted wavelengths, is inside the cavity a faster loss mechanism is observed due to absorption. The CRDS system continuously compares the ring down time of the evacuated cavity with that of the ring down time at the wavelengths that are being absorbed by the gas species (Figure 9).

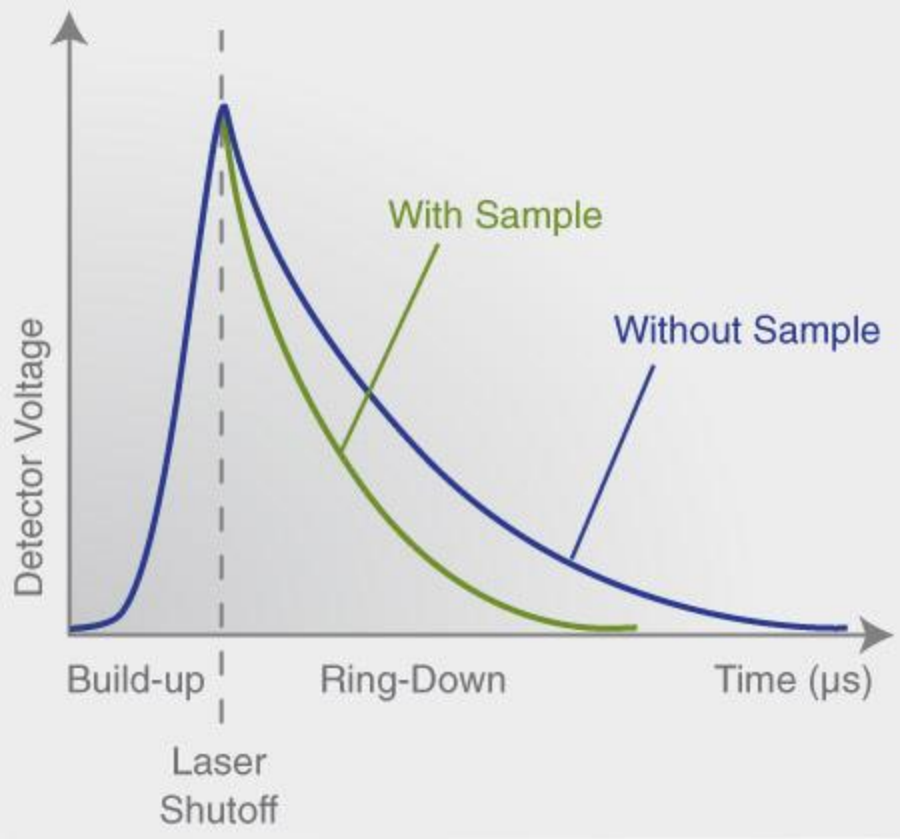

Figure 9; Voltage detected within a CRDS with and without a sample absorbing at a specific wavelength allowing for quantification of target species gas concentration. File from; http://www.picarro.com/technology/cavity_ring_down_spectroscopy

The laser is tuned to a number of wavelengths along the absorbing features of each gas species to fit the shape of the absorption line for each gas concentration. Each wavelength is measured individually, as opposed to scanning an entire absorption line, at a precision 1000 times smaller than the Doppler-broadening linewidth for these gas molecules. In order to produce a meaningful value from these absorptions, measurements are not made until the cavity has reached a constant pressure and temperature. The pressure is reduced and temperature kept slightly above room temperature in order to eliminate the risk of water condensing inside the cavity as well as reduce pressure broadening of ro-vibrational lines which reduces interferences with water and makes cross sections higher at the central

wavelength. As an example the Piccaro instruments will only begin taking measurements with pressure and temperatures of 140 ± 0.07 torr and 314 ± 0.02 K, respectively.

Mathematically the light at the photodetector is

$$I(t,\lambda) = I_o e^{-t/\tau(\lambda)} \tag{16}$$

With I being the transmitted light when the light source is turned off and $\tau(\lambda)$ is the ring down time constant. The empty cavity decay rate is represented as

$$R(\lambda) = 1/\tau_o(\lambda) \tag{17}$$

The decay rate within the cavity is the sum of the empty cavity decay rate and the decay rate due to gas absorption at a given wavelength

$$R(\lambda, C) = \frac{1}{\lambda} = R(\lambda, O) + c\varepsilon(\lambda)C \tag{18}$$

With the effective path length of a measurement being given by the formula below with c being the speed of light

$$L_{eff} = c\tau_o(\lambda) \tag{19}$$

A gas species absorption can be represented as

$$\alpha(\lambda) = \varepsilon(\lambda)C \tag{20}$$

With ε being the extinction coefficient and C being the gas concentration. This absorption can be calculated by finding the difference between decay rates of an empty cavity and a cavity containing a gas species

$$\alpha(\lambda) = 1/c[R(\lambda, c) - R(\lambda, 0)] \quad (21)$$

1.4 Emission Quantification Methods for CH_4

Atmospheric measurements give insight into the concentrations of a pollutant at a very specific point in time and space. In order for more information to be gained from individual measurements, emissions quantification can be carried out. One method is to quantify vertical fluxes through Eddy Covariance where micrometeorological data is used in conjunction with concentration data to determine the vertical flux of emissions (Goulden et al, 1996) from a surface source. These flux measurements can be carried out in a number of ways including using towers where wind speed and direction instruments and gas analyzers will be mounted at fixed heights (Grimmond, 2002). These non-invasive measurements of gas exchange emission fluxes have been conducted in developed urban areas such as Mexico City (Velasco, 2002), Copenhagen (Soegaard, 2003), Vancouver (Walsh, 2004) and Tokyo (Moriwaki and Kanda, 2004) as well as in less polluted rural areas such as Harvard Forest in Massachusetts (Potosnak, 1999) and ongoing monitoring on Mauna Loa by NOAA. These types of flux studies have given insight into seasonal and diurnal trends of emission fluxes of CH_4 (Goulden et al, 1996, Cicerone et al 1983).

Another emissions quantification method known as “tracer dispersion” involves releasing a known amount of a tracer gas over time at the emission site and measuring both the tracer and the suspect gas at a downwind site. The underlying principle is that the tracer gas, often acetylene, N_2O or SF_6, will mix and be diluted into the atmosphere in the same way as the target gas (Czepiel et al 1996 and Galle et al 2001). If the release rate of the tracer gas is well known, then the release rate of the target gas from the

source can be determined using the relative downwind concentrations of the two gases. In one case acetylene (C_2H_2) was released at the site of a landfill and both CH_4 and C_2H_2 were measured (Monster, 2014). If the controlled release of the tracer gas is co-located with the emission site a combination of upwind and downwind measurements allow for the determination of an emission rate. This tracer release method was also used to quantify a very large methane leak in California recently (Herdon et al, 2016).

Various mass balance techniques involving aircraft based measurements have allowed emission measurements from large sources (e.g., a city, large industrial complex, or oil and gas region) to be made by flying downwind of a source perpendicular to the prevailing wind, or around an emission site. This top-down approach allows for calculation of the total integrated emissions from a site, often kilometers wide with multiple emission sources. Many types of aircraft based mass balance measurements of CH_4 have taken place, the most simple being a single-height transect in which one assumes a well-mixed boundary layer with known boundary layer height (Turbnull et al 2009, Karion et al 2013). In these studies a mass balance approach was used in which the enhancement of CH_4 downwind of the source is calculated by subtracting the CH_4 levels upwind of the source. If the horizontal wind speeds are constant from the source of CH_4 to the point of measurement, the mass emission rate from the source can be calculated using the following equation;

$$E = \int_{s-start}^{s-end} \int_{z_o}^{z_{PBL}} \left(\chi_{CH4} - \chi_{CH4,backgnd}\right) U \cdot \cos(\theta) \cdot \frac{P \cdot MW_{CH4}}{RT} ds\ dz \qquad (22)$$

Where U is the mean horizontal wind speed, θ is the angle between the perpendicular to the transect of measurement and the wind direction, $X_{CH4\text{-}bck}$ is the background mixing ratio of CH_4 entering the source region and X_{CH_4} is the downwind mixing ratio of CH_4, integrated over the entire width of a plume (s-start to s-end) and vertically from the ground, Z_o, to the top of the mixed boundary layer, Z_{PBL}. The

pressure, P, temperature, T, molar weight, MW_{CH4} and the ideal gas constant, R as input as constants for each day. If only a single transect is flown downwind far enough that the boundary layer is well mixed, then the vertical integral becomes a trivial solution, multiplication over the height of the boundary layer. This is done presuming air density does not decrease significantly with height, otherwise this can be corrected for assuming adiabatic expansion using integration of the Barometric Law.

An improvement on the single transect approach is to characterize a single screen by flying multiple transects back and forth perpendicular to the wind downwind of the emission site at increasing height in order to capture an entire emission plume passing through a 2-D plane (Camaliza et al 2014). The most involved method of airborne measurements involves box flights around an emission site to enable a mass balance approach to be carried out on the volume within (Alfieri et al 2010). The largest uncertainties with these aircraft mass balance techniques have been shown to be the uncertainties associated with extrapolation of the mixing ratios below the lowest flight level (Gordon et al 2015; Baray et al., 2017) to ground level when one is very close to the source. The lowest height that can be typically flown is 500 ft (150 m) agl in remote regions and 1000 ft (300m) agl in built up areas. It was shown that when a plume is clearly elevated (e.g., from a stack emission) and captured by a flight path the uncertainty is low, however, when emissions are from a ground source, the error associated with a single aircraft based estimate can be as high as 30-50% (Gordon et al., 2015).

1.5 Purpose of Thesis

The purpose of this study is to develop and demonstrate the feasibility of a ground based top-down approach to quantify large emission sources of CH_4 which can be compared with emission inventories that are estimated via bottom-up approaches. Our current study aims to reduce the uncertainty and cost related with aircraft based extrapolated surface concentrations by employing a ground based mobile CRDS to drive single perpendicular transects downwind of the source under conditions when the

boundary layer is well mixed, in conjunction with a stationary TDL system. Our method will build on the aircraft mass balance techniques by making ground level transects where surface concentrations are highest and most important to a source estimate, however we have no vertical information. In order to verify that we are sufficiently downwind of the source for the well mixed assumption, multiple transects are driven at increasing distance away from our emissions site, and comparing the magnitude of the horizontal integral (dx, –b to +b) in Equation 22, as a function of distance away from the source to ensure it has converged.

The aim of this project is to i) characterize the vertical and lateral dilution of the plume and ii) to verify if the furthest transect is sufficiently far enough downwind of the source such that the assumption of complete mixing in the boundary layer can be assumed, so that a total emission rate will be calculated with the assumption that the plume has mixed homogenously throughout the PBL at that point. This methodology was applied to the measurement of CH_4 emissions from the KVL, which we then compared to Emission Inventory estimates.

2.0 Experimental

2.1 TDLAS

Upon acquiring a LasIR RP101 Portable Gas Analyzer TDL from Unisearch (emitting light at 1650 nm) its performance was characterized before being put to use during the Keele Valley Landfill field study. Characterization began with testing the performance of the TDL at increasing separation distances (D) between the TDL telescope and the retroreflector (19-cube, Au coated) to determine the maximum range it could be used at. This took place on a large field located on the York University campus south of the Petrie Science Building. Initially a 30-cube Al coated retroreflector was used, including measurements made at an ECCC station in Egbert, ON. However poor performance was achieved with that retroreflector and a custom 19-cube Au coated retroreflector (Unisearch) was ordered and used in all the measurements discussed here. In all cases the TDL and retroreflector was placed at increasing distances away from each other. The TDL was powered by having a 120 Watt inverter plugged into the cigarette lighter of a car parked 20m downwind of the TDL. Measurements were made with return path lengths, L, (L = 2D) starting at 150m, increasing at intervals of 50m to a maximum of 500m. Path lengths longer than 500m were measured by placing the TDL in the CAC Air Quality Research Station on the 5th floor of Petrie and moving the retroreflector to various spots on campus. The most common path length used with this setup was L = 675m (D = 337 m) by placing the retroreflector in the Osgoode Hall parking lot. The greatest path length tested was L = 1100 m (D=550m) with the retroreflector being at the back of the baseball field south of Petrie with the TDL in the 5th floor lab.

At all of these distances the effect of varying dwell times, the time for an individual data point to be recorded, was also assessed. Dwell times of 0.1, 0.5, 1, 2, 5, and 10 seconds were assessed at each path length. Measurements were made allowing for enough data points to be collected at the longer dwell times to be able to compare their relative noises with shorter dwell times. In doing this, optimal

operating conditions were established at a variety of distances allowing for more flexibility during field studies.

The TDLAS was deployed on two days during the KVL campaign, May 16 and May 17, 2017, 1800m away from the center of the KVL. On both days the TDLAS was powered using a GOAL ZERO Yeti 400 Power Pack for portable power. The TDLAS was focused onto the 19-cube gold coated retroreflector at total return path lengths of 618m and 314m on May 16th and May 17th, respectively. The TDLAS was operated with a dwell time of 0.1 seconds with averaging to longer time taking place during data processing. The TDLAS was calibrated by having the Picarro parked on the road adjacent to the beam path of the TDLAS for 5 minute intercomparison periods. The calibration factor was then applied to the TDLAS data during data processing. These calibrations took place before and after each complete driving run.

2.2 Cavity Ringdown Spectroscopy

A Picarro G2401-m CO/CO_2/CH_4/H_2O CRDS was used to take mobile measurements around the KVL. The Picarro along with a vacuum pump and GOAL ZERO Yeti 1250 Power Pack were secured in the trunk of a SUV. A 4-meter inlet line, with 2.5µm filter, was attached to the passenger side-mirror to allow air sampling to be taken away from emissions from other vehicles on the road. The flow rate of the Piccaro was 454 cm^3/min with CH_4 measurements being made at 1.65 µm. The Picarro data was averaged to 2.5 seconds and instrumental response time was measured at the end of each driving day. The Picarro's response time was measured by exhaling air at a perpendicular angle to the inlet tube. This allowed for the sampling of human exhausted air into the instrument in the same way as the Picarro would normally sample air. The response time was taken as the time between the exhale and the significant peak in H_2O and CO_2. This was done in triplicate to ensure accuracy.

During the drive the CRDS was parked beside the TDL to allow for intercomparison and daily calibration. This calibration was carried out by parking the Piccaro on a street adjacent to the TDL return path for 5

minute intervals before, between and after an entire run on each day. Due to the location of the TDL with respect to the available roads, the calibration took place closer to the TDL than to the center of the TDL path length, which would have been ideal. A calibration factor was derived from the parked periods during times when the wind and CH_4 levels were demonstrating a correlation that emission were travelling from the KVL and crossing the TDLs return path.

The Picarro used during the Keele Valley Landfill field study and preliminary drive was calibrated on March 13, 2017 at Environment Canada using five calibrated gas cylinders. Each cylinder was sampled by the Picarro individually at atmospheric pressure using a tee and an overflow. This was carried out for five minutes for each tank with a constant flow rate from the calibrated CH_4 tanks. This produced a calibration which was applied to all measured CH_4 values during data processing.

2.3 Keele Valley Landfill Field Work

The Keele Valley Landfill study was preceded by an exploratory driving study carried out on November 28, 2016 to identify local sources of CH_4. This earlier work was carried out using the same instrumental setup as the following Keele Valley Landfill drives in April and May 2017. The inlet tube from the Picarro was attached to the passenger side side-mirror to reduce emissions from other vehicles on the road as well as the experimental vehicle. All transects presented here and used for emissions estimates were carried out while driving on the side of the road closest to the KVL. This further ensured that emissions from vehicles immediately downwind of our measurements were not detected. All times when emissions from larger vehicles (most often larger diesel trucks) were detected, those data points were removed during processing. Additionally, the drives were attempted to be carried out at a constant speed to provide the most consistent spread of data.

The vehicle driving the Picarro was also equipped with a Garmin GPS 64s in order to track the vehicles' location. The GPS data was collected at 1 second intervals and had its electronic clock synchronized with the Picarro's clock at the start of each drive. This allowed the GPS data's latitude and longitude of each data point to be correlated with a corresponding CH_4 measurement from the Picarro. This then allowed the CH_4 data to be plotted on Google Maps to be interpreted visually as well as emission estimates to be made.

The preliminary drive consisted of probing two sites of particular interest, the Keele Valley Landfill and a suspected CH_4 leak from a sewer source near Lake Wilcox. The driving route was carried out from York University campus north to the KVL and then towards Lake Wilcox before returning to campus. Upwind measurements of each location were taken prior to each downwind transect to help identify other sources of CH_4.

The Picarro was driven on days with little to no precipitation around the KVL with winds from the south-west, south or south-east (Fig. 10). These wind directions were ideal as they allowed transects to be driven north of the KVL in a rural setting with few additional sources of CH_4. South of the KVL is developed suburban land, which would increase uncertainty in the results due to the presence of additional CH_4 sources. When winds were south-east four transects were driven west of the KVL while south or south-west winds resulted in three transects being driven. The closest transects were often in the range of 2 km while the furthest transect reached 8 km away from the center of the KVL. Transects were driven starting with the closest to the KVL and moving further out in increasing distance from the KVL. The CH_4 flux for each transect was calculated and plotted against distance from the CH_4 source to determine a point at which the plume was fully mixed to the height of the PBL. This acts to determine the distance from the source at which the plume is homogenously mixed, and allows us to determine

the integral at an infinite distance away from the emission source (theoretically at least), fulfilling the fully mixed criterion.

Figure 10; Keele Valley Landfill and surrounding areas. Areas of note are power-plant located at the southern-most edge of the landfill, the landfill site and the location that the Met Station was deployed on all drives

Meteorological data was collected using a 110-WS-25 Modular Weather Station. The weather station was powered with a 10 to 30 Volt DC on-board rechargeable power supply at 20 mA. The weather station had six modules for measuring wind speed, wind direction, temperature, relative humidity, barometric pressure and precipitation. The precipitation module was removed during all field study days as no measurements were taken on days with rain and the weight of the module caused complications during periods with high winds. The Met station was secured to the earth using two 9-inch nails into each of the tripod legs and was deployed on all days of the driving study on a flat field directly west of

the KVL (Fig. 10). The field was on top of a reservoir elevated ~ 10m above the surrounding terrain. The on-board clock was calibrated to match that of each data point from the Picarro allowing for correlation of wind speed and direction to take place during data processing.

3. Results

3.1 Analytical Performance of TDL

The TDL had its performance characterized on campus prior to use during the Keele Valley Landfill field study. In order to understand the impact of varying the dwell time of the TDL, measurements were taken, at a return path of 498m, at dwell times of 0.1, 0.5, 1, 2, 5 and 10 seconds (Fig. 11). These measurements were taken on a baseball field on York University campus and are summarised in Table 1 showing the standard deviation (σ) of data within a given dwell time bin and standard error of the mean. Longer dwell times allow more absorption scans to be averaged, where the number of scans would be proportional to the dwell time. Theoretically one would expect that the noise would be inversely proportional to the square root of the number of averaged scans, and therefore also inversely proportional to the square root of the dwell time. This can be explained through the relation of standard error of the mean, $\sigma_{\bar{X}}$, being equal to the standard deviation, σ, divided by the square root of the sample size, N.

$$\sigma_{\bar{X}} = \frac{\sigma}{\sqrt{N}} \tag{23}$$

As seen in Table 1, the standard deviation decreases as the dwell time increases as expected (Fig. 12). The characterization of the TDL showed a trend of decreasing noise, σ, as dwell time increased (Table 1). The noise decreased by a factor of 4.7 (as do the detection limit, 3σ and limit of quantification (LOQ), 10 σ) as dwell time increased by a factor of 100 from 0.1 second to 10 seconds, compared to a theoretical expectation of a decrease in noise by a factor of 10, if there were no other sources of noise.

In order to maintain high time resolution data, it was decided to take measurements with the lowest possible dwell time and average the results during data processing during field studies. This would allow

any short temporal trends to be captured while maintaining low noise in the data. This was shown to be a viable option by averaging bins of 100 measurements at 0.1 second dwell time to 10 seconds bins and comparing to the standard deviation of measurements made with a dwell time of 10 seconds (Table 1, far right column). This averaging resulted in a LOQ, the lowest mixing ratio in a sample to be quantified, of 0.48 ppm as compared with the un-averaged 10 second measurement which had a LOQ of 0.43 ppm.

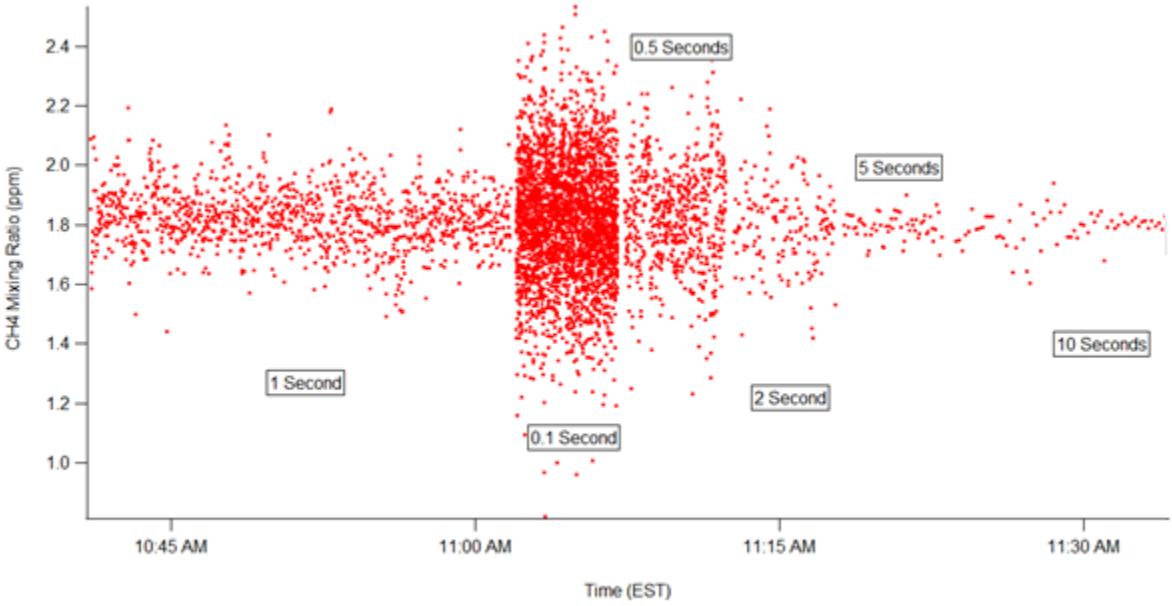

Figure 10: TDLS characterization of noise through dwell time analysis.

Table 1: Impact of Dwell time on the noise of the TDL measured at a return path length of 498m. * This column represents the bin of 100 measurements taken at 0.1 seconds to be compared with the noise of measurements taken at 10 seconds

Dwell Time (sec)	0.1	0.5	1	2	5	10	100 bins of 0.1 seconds*
Average CH_4 (ppm)	1.82	1.82	1.82	1.80	1.79	1.79	1.82
Standard Deviation	0.20	0.16	0.10	0.14	0.04	0.04	0.045
3σ (LOD)	0.61	0.50	0.29	0.41	0.12	0.13	0.145
10σ (LOQ)	2.02	1.67	0.97	1.36	0.41	0.43	0.489
1/sqrt(dwell time)	3.16	1.41	1	0.70	0.45	0.32	

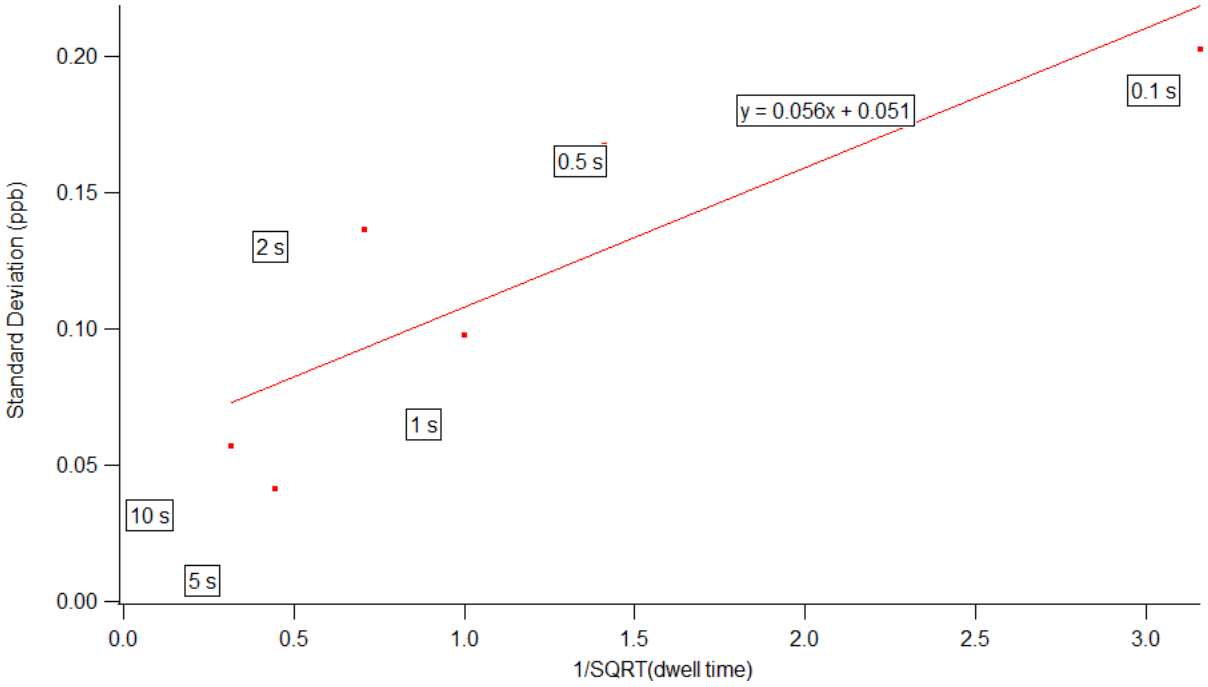

Figure 112; Shows the noise associated with each data point as Standard Deviation is proportional to 1/√dwell time

3.2 Analytical Performance of Picarro

The Picarro used during the Keele Valley Landfill field study was calibrated on March 13, 2017 at Environment Canada using five calibrated gas cylinders. Each cylinder was sampled by the Picarro at atmospheric pressure using a tee and an overflow, for five minutes using a constant flow rate from the CH_4 tanks. The observed vs. reported mixing ratios are plotted in Figure 13, with a regression slope of 0.99 ± 0.01 with an x-intercept equal to zero within error, b = 0.014 ± 0.020 ppm. Thus there was no statistical difference between the observed and expected mixing ratios. Nonetheless, a small correction to all data points was performed as a result of this calibration. Each data point of CH_4 was divided by the slope which acted as the applied calibration factor. This was carried out as the x-intercept was zero within error.

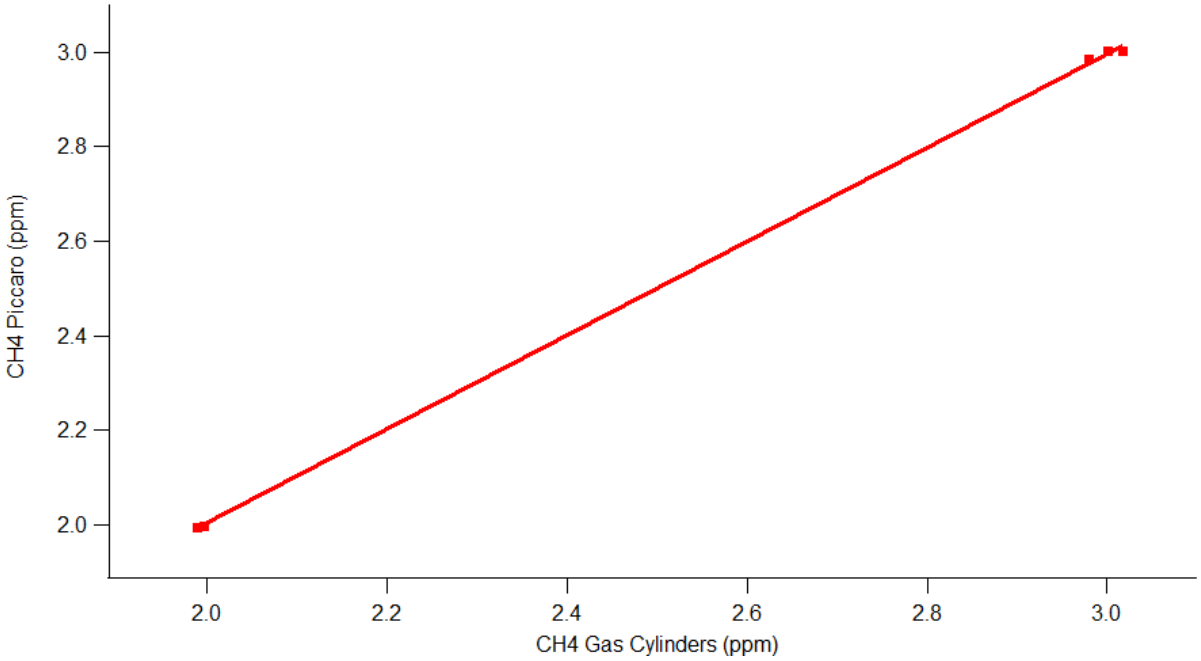

Figure 13; Piccaro calibration using 5 calibrated gas cylinders at ECCC on March 13, 2017.

Using CH_4 data measured by the Piccaro on October 8 2017 the noise and 3σ can be compared with that of the TDL. The 3σ value for the Piccaro was 0.0047 ppm for an average CH_4 mixing ratio of 1.9094 ppm measured over a one hour time period. Comparing this 3σ value to that of the TDL (0.408 ppm) for the same dwell time of a measurement shows that the noise is lower on the Piccaro by two orders of magnitude. This will allow the Piccaro to detect smaller changes in CH_4 mixing ratio over a shorter period of time and be the primary instrument to carry out the most accurate emission estimate calculations.

3.3 Preliminary Driving Study

On November 22, 2016 a preliminary driving study was carried out to identify local sources of CH_4. Our target destinations were the Keele Valley Landfill in Vaughan and a community reported odorous sewer source in Oak Ridges, ON; separated by just a few kilometers (AECOM, 2017). It is known that sewer

sources of odours are frequently H_2S gas, which is often co-emitted with other products of anaerobic digestion of organic material such as CH_4 and other organic sulfides. The winds on this day were roughly from the southwest, leading us to expect enhancements of CH_4 on the east side of any sources. A driving route was carried out from York University campus north to the KVL and then towards Oak Ridges around the suspected sewer source, before returning to campus (Fig. 14) past the KVL again. Upwind measurements at each location were taken prior to each downwind transect to help identify background levels of CH_4 and any other sources. Figure 16 shows multiple northbound and southbound downwind measurements of the KVL. During the initial northbound transect the entire plume was not detected. A second and complete northbound transect detected a maximum CH_4 mixing ratio of 3.3 ppm. With a background of ~ 1.95ppm, the landfill enhancement was about 1.35 ppm (1350 ppb).

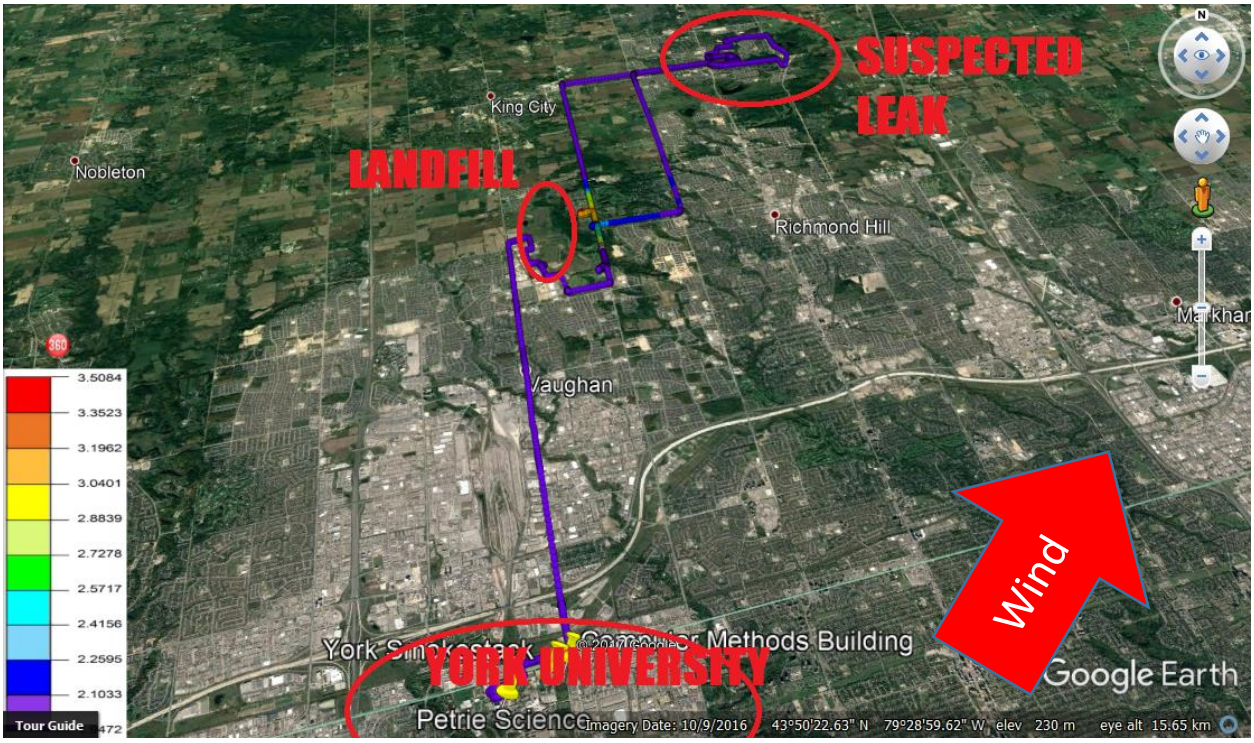

Figure 14. CH_4 data from Nov 29, 2016 driving study from York University campus to qualitatively identify CH_4 sources

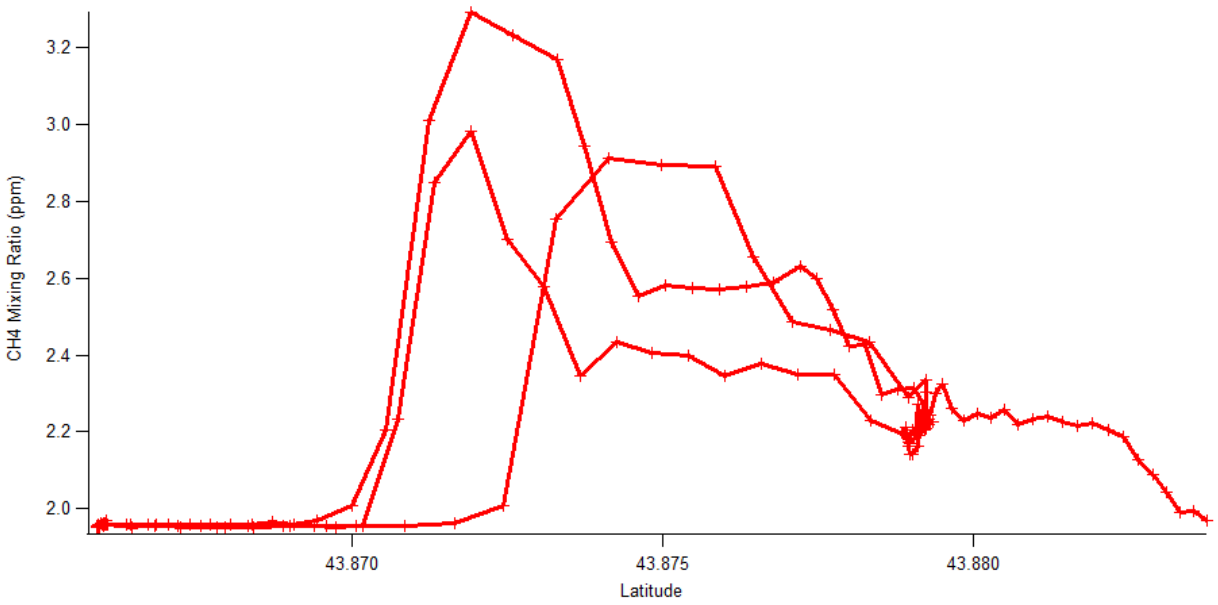

Figure 15; CH_4 mixing ratios on November 22, 2016 plotted against latitude to show the back and forth driving downwind of the KVL plume.

The drive to Lake Wilcox did not identify any significant sources of CH_4 nor did driving downwind of the suspected CH_4 leak area. Figure 16 shows the time series data of the CH_4 mixing ratios when circling the roads close to Lake Wilcox east of Yonge Street in Oak Ridges from 3:45-4:00pm, downwind of the suspected CH_4 source emanating from sewers coincident with odours in the area (likely H_2S). The highest CH_4 mixing ratio was just over 2.01 ppm, an enhancement of ~ 60ppb. If a CH_4 source did exist, it was indeed minor compared to the source of CH_4 from the KVL. After this observation, we decided to focus on the KVL source of CH_4.

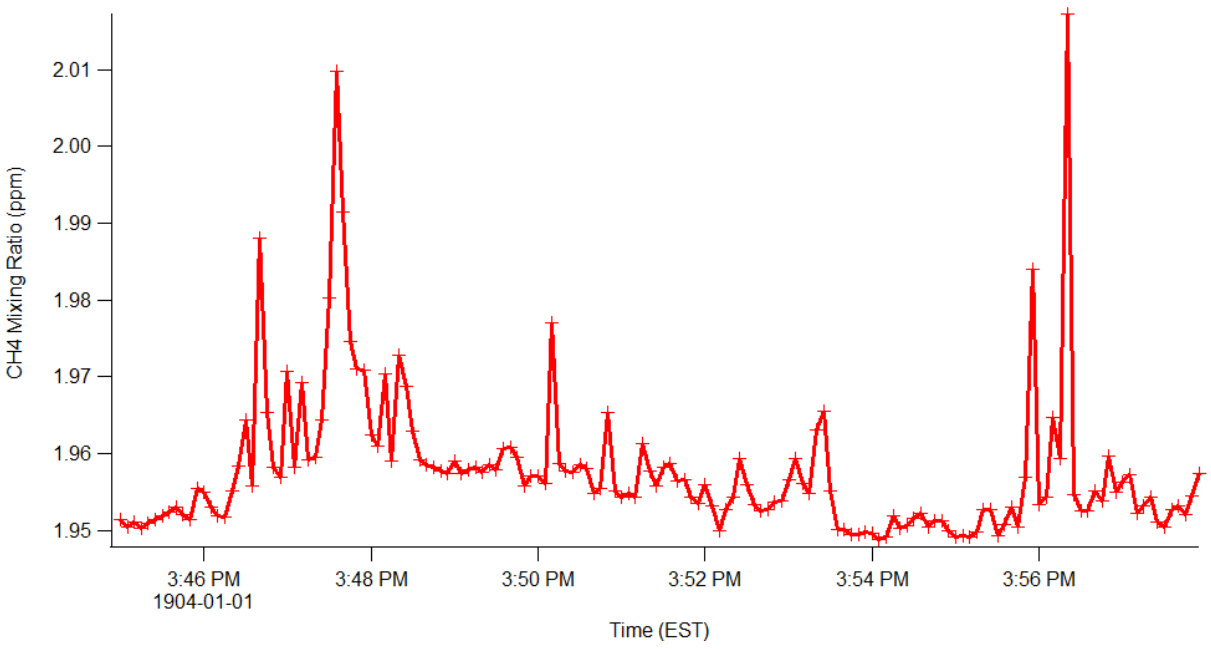

Figure 16. Driving downwind of suspected CH_4 sewer source in Oak Ridges, ON

The time series for the drive southbound past the KVL approximately two hours after the first northbound transect is shown in Fig 17 and is the fourth transect driven that day. The peak had a total width of roughly 2000m with the transect being measured while the car was travelling at 30 km/hr with the enhancement lasting nearly four minutes. The profile of the KVL emission on this day showed an elevated peak at the southernmost region and a plateau north of it. The southernmost peak was attributed, through back wind trajectories, to the power generating station while the enhanced plateau region was associated with CH_4 seeping through the soil now covering the landfill. There is an underground gas collection system at the KVL which funnels CH_4 to the power station where it is used to produce electrical power. The CO_2 in this area was variable and not coincident with the CH_4 enhancement; but if so it is buried within the CO_2 from roadside noise. If combustion was taking place it would be expected to see an incident increase in CO_2 with CH_4 however this was not observed (Figure 17). This led to the idea that the gas was still being collected and then vented from the power station

instead of being used to generate power or flared. Upon driving the southbound transect past the KVL the highest CH_4 detected was 4.8 ppb. This increase in enhancement (~2.8 ppm above background) compared to that seen two hours prior (~1.3 ppm above background) was attributed to the PBL decreasing in height as the sun was setting.

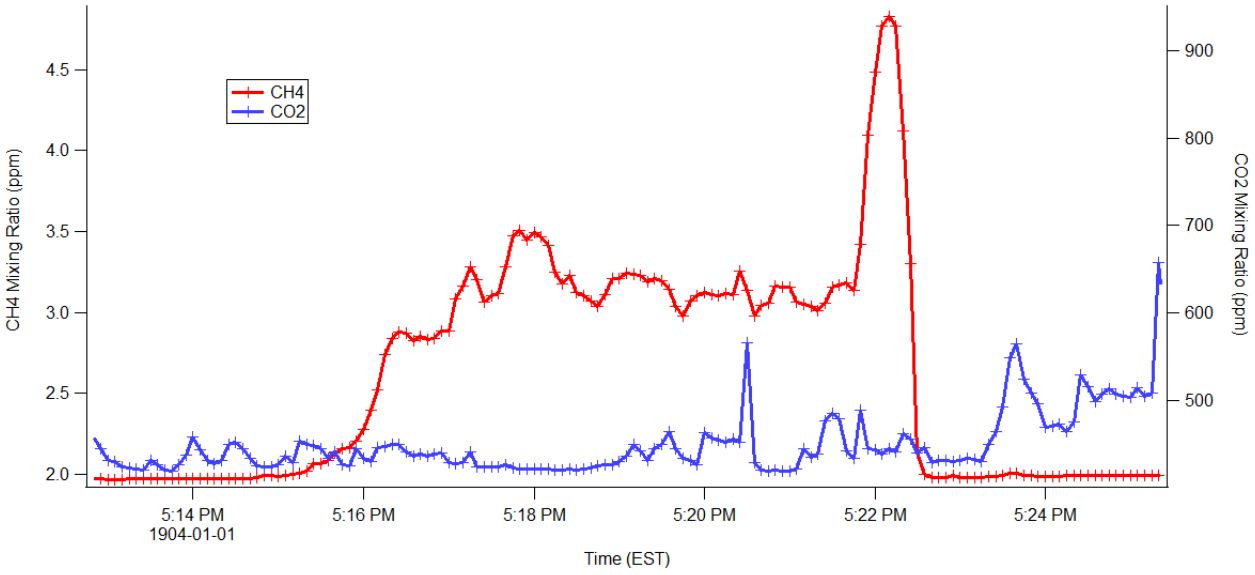

Figure 17. Southbound transect east of the KVL on November 24, 2016 showing CH_4 and CO_2 levels. CO_2 levels were not enhanced which would be expected if the CH_4 was being combusted as previously reported.

3.4 Keele Valley Landfill Field Study

The KVL field study took place on April 26-28 and May 16-17, 2017. On each of these days the Picarro was driven with transects downwind of the KVL with the TDL being deployed stationary on the May 16 and May 17 dates. Table 2 summarizes the wind conditions for each day and results of each run. Each run is further subdivided into multiple transects (Table 2). Runs which had poorly defined plumes were eliminated from any further data processing including; April 28 Run 1, April 28 Run 3 and May 16 Run 2.

Table 2; Summary of characterization of each driving transect

Date	Run	Driving Direction	Wind Direction	Transects
April 26	Run 1	NB, west of KVL	SE	4, well defined
April 26	Run 2	NB, west of KVL	SE	4, well defined
April 27	Run 1	NB, west of KVL	SE	T1 clear, T2 & T3 noisy
April 27	Run 2	EB, north of KVL	S	T1 clear, T2 & T3 noisy
April 28	Run 1	SB, east of KVL	SW	T1, T2 clear, T3/T4 noisy
April 28	Run 2	SB, east of KVL	SW	T1 clear, T2/T3 noisy
April 28	Run 3	SB, east of KVL	SW	All noisy
May 16	Run 1	EB, north of KVL	S	3, well defined
May 16	Run 2	EB, north of KVL	S	All noisy
May 17	Run 1	SB, east of KVL	SW	T1/T2 clear, T3 noisy
May 17	Run 2	SB, east of KVL	SW	3, well defined

The CH_4 mixing ratios from the days with well-defined plumes were plotted spatially using the GPS data to produce visual maps of the CH_4 enhancements around the landfill (Figures 18 and 19). The CH_4 enhancement on April 26, 2017 and May 16, 2017 are overlaid on top of Google Earth, as examples, to show the location of enhancement relative to the KVL. These plots allowed for winds to be used for back trajectory or identification of the power plant and landfill sites as the major CH_4 emitters. On May 16th the TDL was also deployed and used to measure CH_4 levels very close to the KVL.

Each run also had the CH_4 plotted as mixing ratio vs distance along each individual transect (Figure 19) by converting the GPS coordinate data to distance along the relevant roadway. This allowed a visualization of the magnitude of the CH_4 enhancement and horizontal spread of the plume as distance away from the KVL increased. An arbitrary starting point of zero distance was chosen for each transect. This point was chosen to allow the complete plume to be shown with background levels of CH_4 being detected before and after the enhancement.

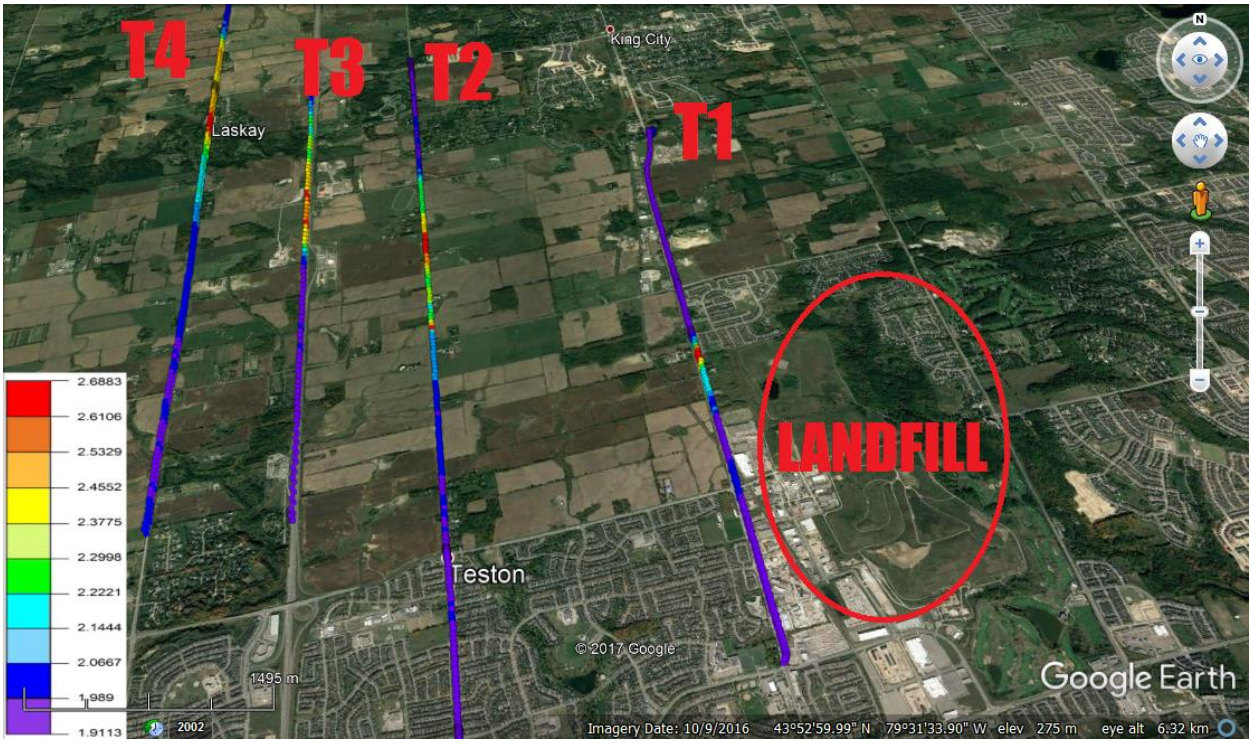

Figure 18; CH_4 mixing ratios for NB transects driven west of the KVL on April 26 2017. Each transect is on its own color gradient to more strongly illustrate the location of the enhancement. The color chart shown is for the T1 transect.

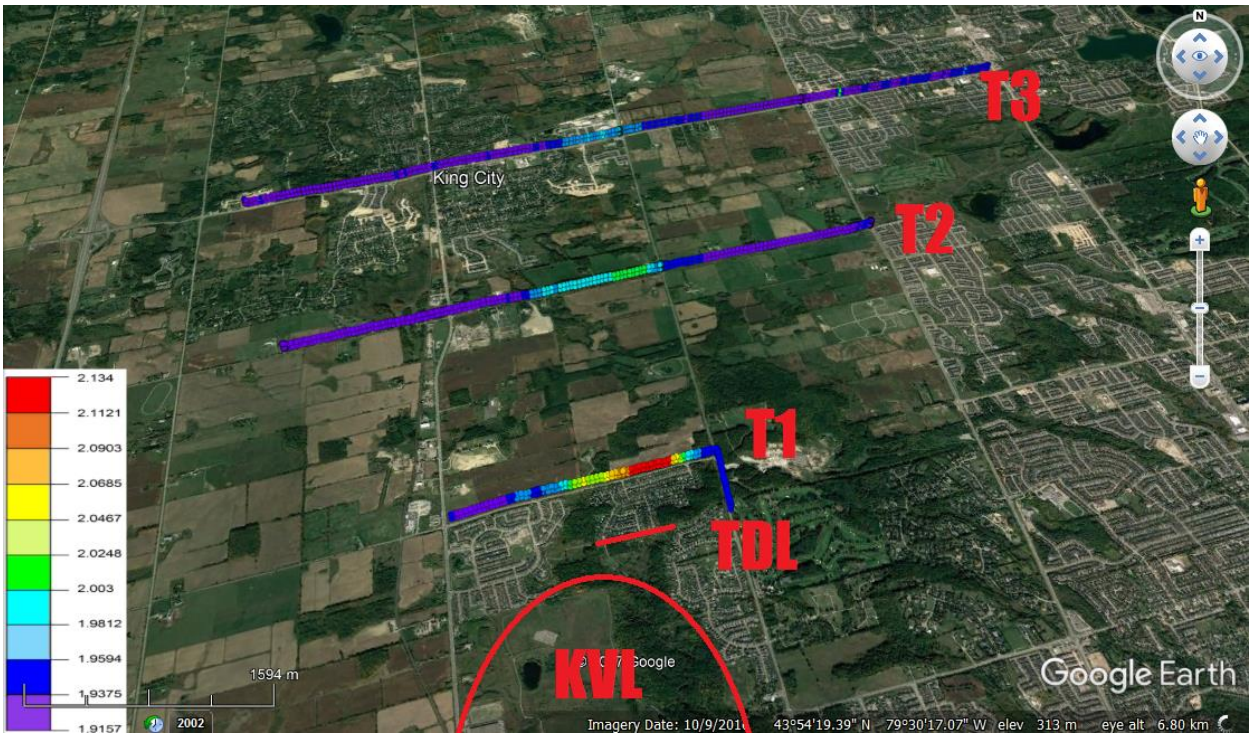

Figure 19; CH_4 mixing ratios on May 16 2017 with eastbound transects north of the KVL capturing SSE winds. The solid red line is the location of the TDL return path during the runs. The color chart shown is for the T1 transect.

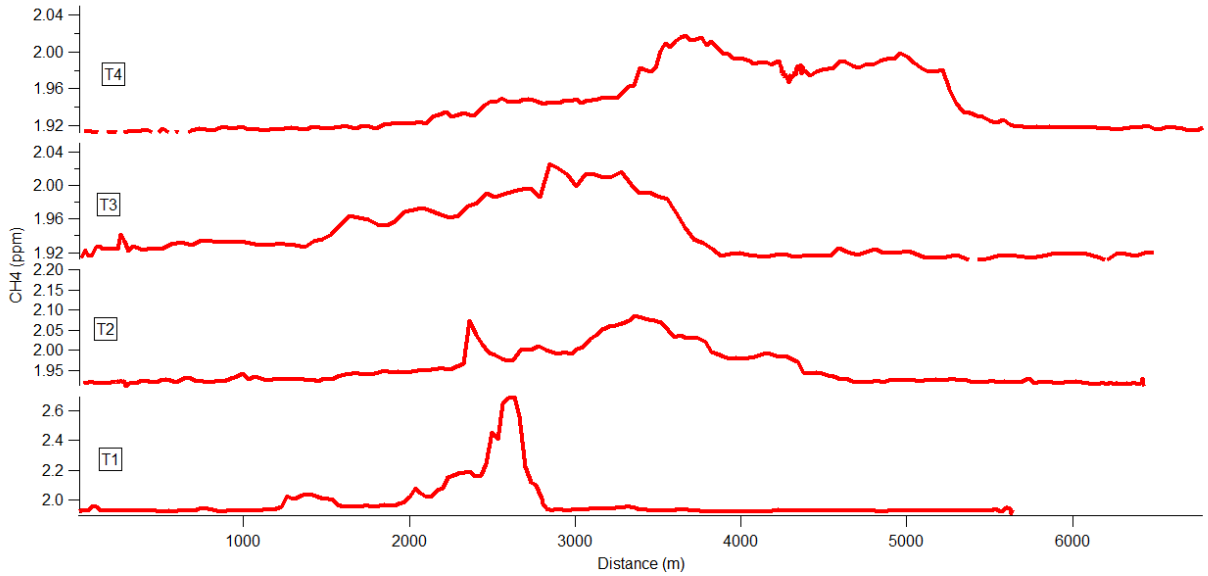

Figure 20; April 26, 2017 CH_4 plotted against distance from the start of each individual transect. Distance along the wind trajectory from the center of the KVL are as follows; T1 is 2440m, T2 is 5170m, T3 is 6550m and T4 is 8950m. Each transect had its distance from zero chosen from an arbitrary point which allowed the entire plume to be shown.

A linear interpolation of the background from the start to end of the period of enhancement was used to calculate the increase in CH_4. A Riemann sum approximation was used to determine the area of the integral.

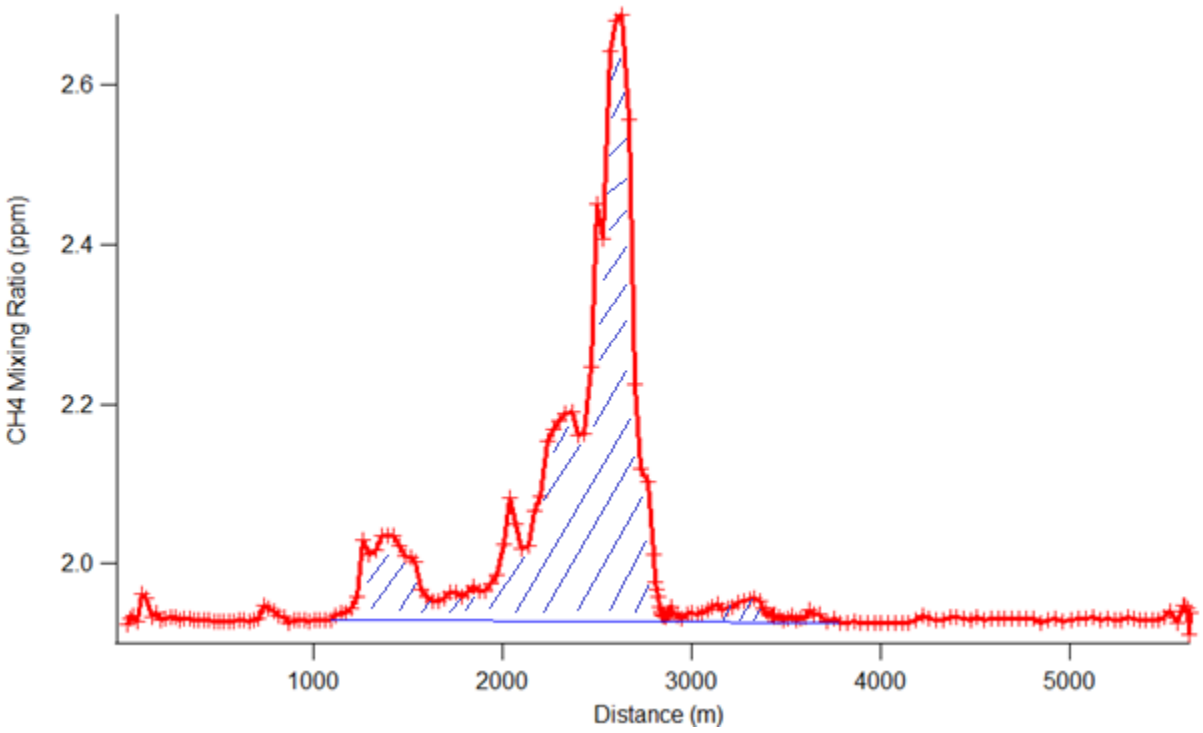

Figure 21; Example of Integration enhanced CH_4 from April 27 2017 – Run 1. The linear blue line represents a linear interpolation of the background CH_4 levels.

3.5 Calculation of Emissions of CH_4 from KVL

By combing the meteorological data collected from the deployed met station and solar intensity data retrieved online the CH_4 measurements were used to calculate emission estimates. This calculation combined wind speed and wind direction along with PBL data through the following formula.

$$E = \int_{s-start}^{s-end} \int_{z_o}^{z_{PBL}} \left(\chi_{CH4} - \chi_{CH4,backgnd}\right) U \cdot \cos(\theta) \cdot \frac{P \cdot MW_{CH4}}{RT} ds\ dz \quad (23)$$

Emission estimates were calculated by first finding the integrals of the CH_4 enhancement along each transect, db, driven for a given day, $\int_{s-start}^{s-end}(X_{CH_4} - X_{CH_{4bk}})ds$. In order to do this the GPS data was used to calculate the distance between consecutive measurement points. This conversion is commonly carried out in one of two ways; either through a Pythagorean Theorem ratio by first converting GPS coordinates to UTM coordinates or by using the Haversine formula, the latter being what was chosen here (Brummelen, 2013). The background CH_4 was calculated using a linear interpolation between the start and end of the enhanced region along the transect, to account for the $X_{CH_{4bck}}$ values. These enhancements were always verified to be reasonable by comparing with T_o, background transects, driven upwind of the KVL. This linear interpolation method was chosen due to differing background levels on either side of the KVL enhancement plume, often separated by several kilometers.

The integral was calculated using a simple Riemann Sum. This integral, $\int_{s-start}^{s-end}(X_{CH_4} - X_{CH_{4bk}})ds$, was then used for emission estimate calculations (Eq. 23). Once the integrals for all of the transects were calculated a plot was created based on the integrals of CH_4 mixing ratio against the distance of a particular transect away from the KVL (Figure 22). The graph shows a decrease in the integral as distance increases away from the KVL (Table 3). Simultaneous is a decrease in CH_4 mixing ratio enhancement away from the KVL (Figure 23). The closest CH_4 mixing ratio on this day was the TDL which had a path length of nearly 250m, one way, which was not long enough to capture the entirety of the plume resulting in a lower value than the highest value detected in the closest transect. The decrease in mixing ratio as distance increases away from the source can be explained by both vertical and horizontal dilution of the CH_4 emissions. The decrease in the integral is explained only by vertical dilution of the plume throughout the planetary boundary layer. The lateral (horizontal) dilution of the plumes is shown

in Tables 5 - 10. The errors associated with each integral come from changing the starting and end point for their calculation. The starting and end points were increased and decreased by 100m. The transects which have the largest error associated with them, T3 on April 27 2017 Run 2, were often from the transects furthest from the KVL. This introduced more time for the CH_4 to mix into the atmosphere and measurements to, possibly, detect other local CH_4 sources. Runs on days that had more variable winds had higher relative errors, as seen on May 16th and 17th.The integral from the furthest distance transects were used in the calculation of CH_4 emissions, as discussed in greater detail using equations 24 and 25.

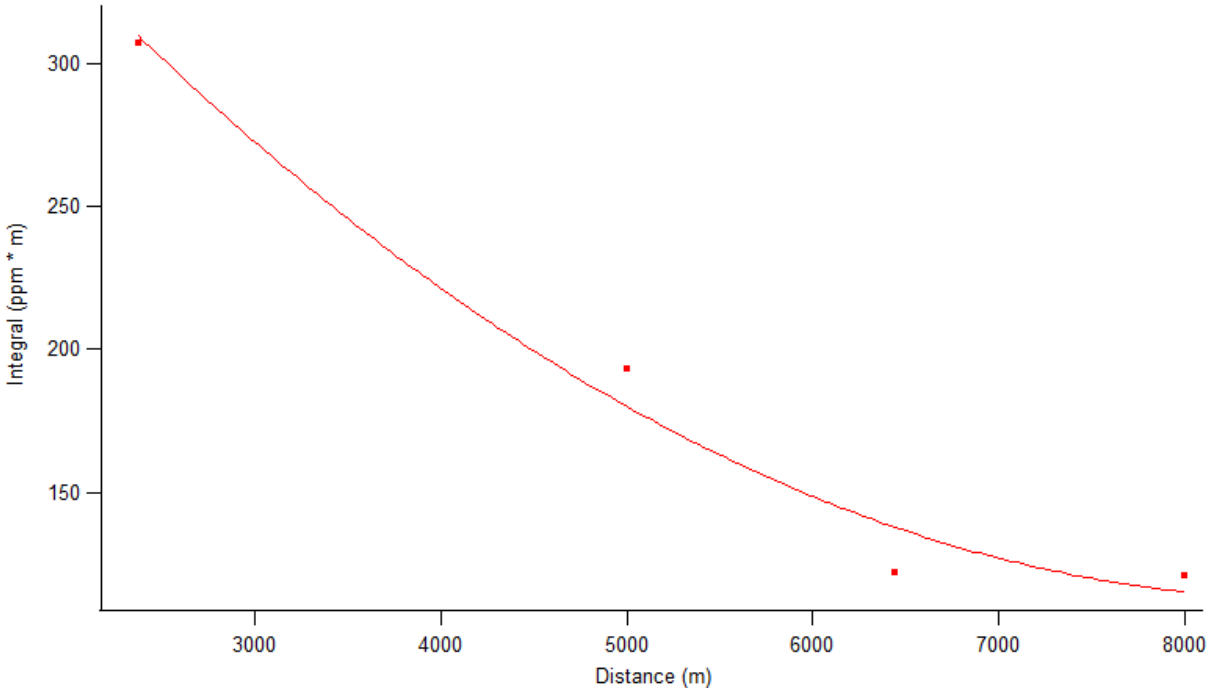

Figure 22; Plot of CH_4 enhancement integral, from April 26 2017 – Run 1, against distance away from the KVL. Distance was measured from a point at the center of the landfill along a straight line crossing all transects. The solid red line is an arbitrary exponential fit illustrating to decay and convergence of T3 and T4.

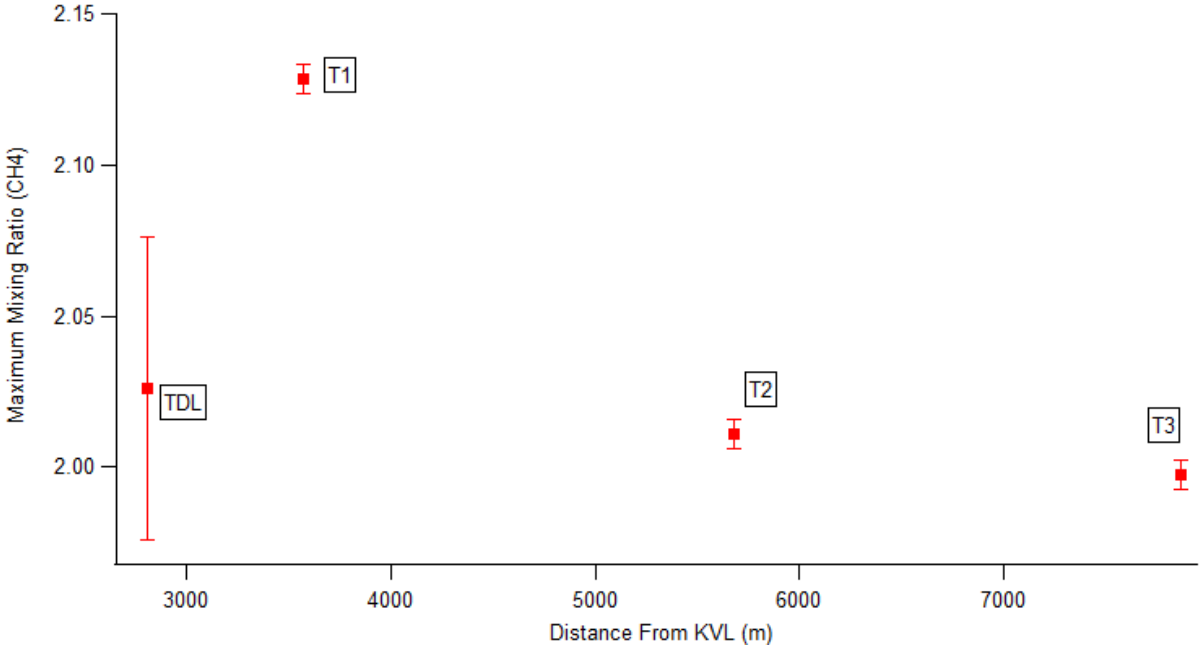

Figure 2312; Maximum CH_4 mixing ratio vs distance away from the KVL on May 16 2017. The distance were measured using Google Earth from the center of the KVL to the peak location of a transect

Table 3; Summary of Distance away from the KVL and a given transects overall CH_4 integral

April 26 2017 - Run 1 (NB - West of KVL)	T1	T2	T3	T4
Distance from KVL (m)	2375	5000	6440	8000
Integral (ppm*m)	307±15	193±17	122±22	121±14
April 26 2017 - Run 2 (NB - West of KVL)				
Distance from KVL (m)	2440	5170	6550	8950
Integral (ppm*m)	298±12	232±10	198±11	119±10
April 27 2017 - Run 2 (EB)				
Distance from KVL (m)	3630	5820	7830	
Integral (ppm*m)	110±10	49±17	41±22	
May 16 2017 - Run 1 (EB)				
Distance from KVL (m)	3570	5680	7860	
Integral (ppm*m)	153±7	81±9	54±18	
May 17 2017 - Run 1 (SB - east of KVL)				
Distance from KVL (m)	3080	5030	7305	
Integral (ppm*m)	222±9	67±9	49±15	
May 17 2017 - Run 2 (SB - east of KVL)				
Distance from KVL (m)	3080	5030	7305	
Integral (ppm*m)	226±2	90±15	49±15	

The values for $\int_{Z\ ground}^{Z\ PBL} dz$, was assumed to be equal to the height of the Planetary Boundary Layer above ground level multiplied by a constant air density of air at ground level, n_{air}. This assumption, as discussed previously, assumes that the horizontal enhancement integral, is determined at a distance sufficiently far from the KVL that the enhanced CH_4 plume is homogeneously mixed in the PBL. The values of the PBL height agl were estimated using Aircraft Meteorology Data Relay (AMDAR) data, taken from an online NOAA database (https//amdar.noaa.gov/). The values retrieved from the NOAA website are temperature profiles measured by commercial aircraft as they are either ascending or descending at local airports. The temperature profiles were used to determine the height of the boundary layer (Oke, 2006) by estimating the height of the inversion layer. An example temperature profile is shown below. The height of the PBL in this case is 4820 ft above sea level (asl), which was then converted to height above ground level (agl) by subtracting the height of the particular airport. Data were collected through this process for each day for time periods during each run. Due to the limited number of flights which reported data through the AMDAR website, data from Buffalo (BUF), Rochester (ROC), Ottawa (YOW) and Montreal (YUL) were needed to be used to estimate the PBL at the KVL. The final PBL heights reported (in summary Tables 6 – 11 below) are distance weighted (from KVL) averages from as many flights as were available (Table 4). Errors for each reported PBL height was calculated by taking the standard deviation of the boundary layer heights for a given day. It is assumed that the PBL is terrain following such that the PBL (agl) detected at another airport would be representative of what was occurring at the KVL. The values for air density, n_{air}, molar mass of CH_4 and Avogardro's Number, A_v, were included in Equation 23 as constant values.

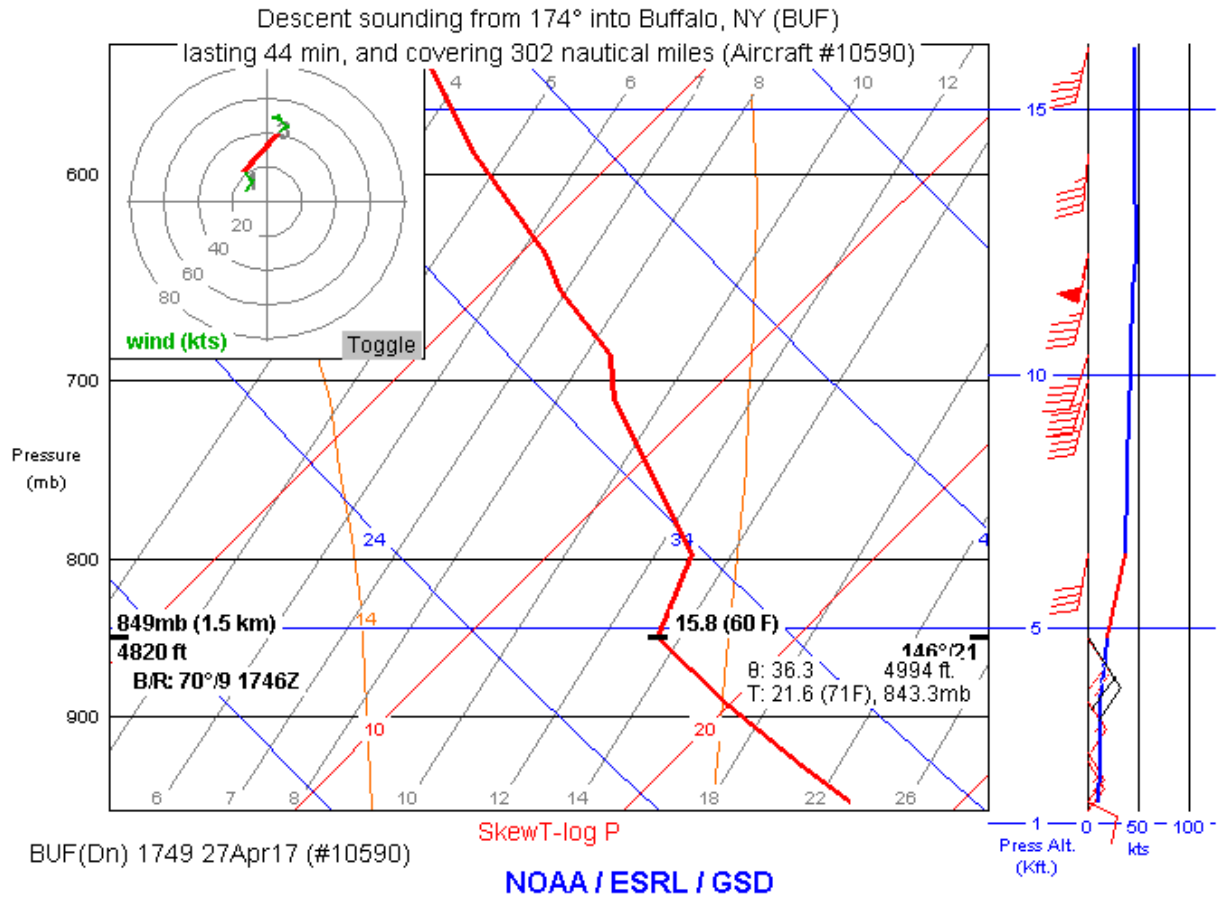

Figure 24; Temperature profile for flight landing in BUF airport at 1749 on April 27 2017. Highlighted temperature data point (red line) is at the height (seen in black on the left axis) at which we determined the PBL to be at this time.

Table 4; Summarizing the data used to calculate the distance averaged means for each PBL height summarized in Tables 6 - 11

Airport - Date	Time (DST)	PBL Height (m)
BUF - April 26	11:58	737.1
BUF - April 26	12:27	716.1
BUF - April 26	12:30	650.1
BUF - April 26	12:40	722.1
BUF - April 26	14:51	674.1
BUF - April 26	15:07	731.1
BUF - April 26	16:18	842.1
BUF - April 26	16:52	689.1
ROC - April 26	10:43	522.6
ROC - April 26	11:45	684.6
ROC - April 26	12:34	546.6
BUF - April 27	11:53	956.1
BUF - April 27	12:42	1220.1
BUF - April 27	13:49	1226.1
BUF - April 27	14:38	1067.1
YUL - April 27	15:54	1323.6
BUF - May 16	10:22	128.1
BUF - May 16	12:25	179.1
BUF - May 16	13:18	215.1
ROC - May 16	10:43	180.6
ROC - May 16	11:36	249.6
ROC - May 16	12:38	135.6
ROC - May 17	10:34	1622.1
ROC - May 17	10:02	1757.1

Wind speed, V, and wind direction were both collected using the deployed met station. Wind speed was reported by the met station in 1 second averages. These values were then further averaged to correspond with the time that an individual transect was driven. The wind speed and direction used in emission estimate calculations were averaged over the course of the overall run in order to account for instrumental noise and more accurately represent the wind during that time. Wind direction allowed for the calculation of the θ value, which was the angel between the wind and normal to the transect direction (i.e. - road direction). Wind speed and direction data was determined to be reasonable by

comparing with publically reported meteorological stations in Vaughan and York University's EMOS systems (http://www.yorku.ca/pat/weatherStation/index.php).

In order to determine which transect, or combination of transects, to use for the emission estimate calculation, the buoyancy flux was calculated for each day. Previous studies have presented the calculation to find the amount of time, t_m, required for a ground based emission source to become mixed homogenously to the height of the PBL, Z_{PBL} (Karion et al. 2013). This was done by first finding the buoyancy flux, w^*, for a given day and time.

$$w^* = [\frac{g z_{PBL}}{\overline{\theta_v}} (\overline{w'\theta_v'}]^{\frac{1}{3}} \quad (24)$$

In this formula g is the gravitational constant, $\overline{\theta_v}$ is the mean virtual temperature and $\overline{w'\theta_v'}$ was the measured heat flux at the surface. The values for $w'\theta_v'$ were retrieved from a privately operated local monitoring station as solar intensity in Watts/m^2 (http://www.vaughanweather.com/wxstation/wxwuhistory.php). The monitoring station was located less than three kilometers south of the KVL and used a Davis Vantage Pro 2 system to record their data. The data was retrieved from their online archive system with time resolution of 1 minute per data point. The retrieved values were converted to buoyancy flux, $\overline{w'\theta_v'}$ (kinematic units of K m s^{-1}), allowing the distance away from the KVL for homogenous mixing to be calculated as these values were assumed turbulent heat fluxes from this incoming radiation. This was done by first finding the mixing time t_m;

$$t_m = \frac{PBL}{w^*} \quad (25)$$

It has been shown that a value of $3t_m$ is the distance away from an emission site where an emission will be homogenously mixed to the height of the PBL (Karion et al. 2013). The required distance was calculated by multiplying the wind speed by $3t_m$. Their values on a sunny day was a t_m of 16 minutes with a PBL of 1250 m while we observed a t_m of 5.5 minutes with a PBL of 664 m on April 26 2017.

The data collected from the field study is summarized in Tables 5 – 10. All emission estimates were calculated using Equation 23 and the resulting values are in Table 11. Due to an inconsistency in the theoretical distance for a homogeneously mixed PBL a discussion on the integral used for each day's emission estimate will follow.

Table 5; Summary of data used for emissions estimate for April 26 2017 Run 1.

April 26 2017 - Run 1 (NB - West of KVL)	T1	T2	T3	T4	Emission Estimate
Distance from KVL (m)	2375	5000	6440	8000	
Integral (ppm*m)	307±15	193±17	122±22	121±14	121
Width of Plume (m)	1776	3295	2513	3857	
Wind Speed (m/s)	2.22±0.1	2.5±0.1	3.4±0.2	3.6±0.1	2.93±0.26
Wind Direction	109 ± 2	141±19	120±1	99.5±9.5	117.4 ± 21
Theta					42.37
Cos Theta					0.738
PBL Height (m)					664 ± 91
Pressure (Pa)	1007.7	1007.4	1007.3	1007.3	1007.4 ± 0.2
Solar Intensity (watts / m^2)	443±16	440±26	448±10	440±20	442.8 ± 38
Buoyancy Flux (K m s^-1)					0.364
w*					1.99
tm (sec)					332
3 tm(sec)					997
Homogenous PBL Distance (m)					3592

Table 6; Summary of data used for emissions estimate for April 26 2017 Run 2.

April 26 2017 - Run 2 (NB - West of KVL)	T1	T2	T3	T4	Emission Estimate
Distance from KVL (m)	2440	5170	6550	8950	
Integral (ppm*m)	298±12	232±10	198±11	119±10	119
Width of Plume (m)	2881	4684	4826	4614	
Wind Speed (m/s)	2.2±0.2	2.7±0.5	1.9±0.7	1.7±0.7	2.2±1.1
Wind Direction	131±9	144.5±4.5	148.5±0.5	129.5±18.5	105.5 ± 21
Theta					63.5
Cos Theta					0.446198
PBL Height (m)					664 ± 91
Pressure (Pa)	1006.3	1006.3	1006	1006	1006.2 ± 0.2
Solar Intensity (watts / m^2)	478±79	498.5±30.5	580±51	551.5±32.5	526.8 ± 104
Buoyancy Flux (K m s^-1)					0.433
w*					2.11
tm (sec)					313
3 tm(sec)					941
Homogenous PBL Distance (m)					3390

Table 7; Summary of data used for emissions estimate for April 27 2017 Run 2.

April 27 2017 - Run 2 (EB)	T1	T2	T3	Emission Estimate
Distance from KVL (m)	3630	5820	7830	
Integral (ppm*m)	110±10	49±17	41±22	41
Width of Plume (m)	1926	1674	3070	
Wind Speed (m/s)	4±1.3	8	1.5±0.6	3.4 ± 2.6
Wind Direction	155.5±19.5	147±1	193±7	165 ± 20.7
Theta				182.16
Cos Theta				0.99
PBL Height (m)				1157 ± 112
Pressure (Pa)	1002.3	1002.3	1002.3	1002.3
Solar Intensity (watts / m^2)	1041±34.5	899±13	888±5	942.7 ± 37
Buoyancy Flux (K m s^-1)				0.775
w*				3.09
tm (sec)				374
3 tm(sec)				1123
Homogenous PBL Distance (m)				1684

Table 8; Summary of data used for emissions estimate for May 16 2017 Run 1.

May 16 2017 - Run 1 (EB)	T1	T2	T3	Emission Estimate
Distance from KVL (m)	3570	5680	7860	
Integral (ppm*m)	153±7	81±9	54±18	54
Width of Plume (m)	1794	2700	2355	
Wind Speed (m/s)	1.8	1.1±0.6	1.8	1.6 ± 0.6
Wind Direction	176.5±4.5	155.5±11.5	135.5±34.5	155.8 ± 36.6
Theta				172.83
Cos Theta				0.99
PBL Height (m)				180 ± 57
Pressure (Pa)	1016.8	1016.5	1016.1	1016.4 ± 0.3
Solar Intensity (watts / m^2)	182±8	184.5±18.5	328.5±3.5	231.7 ± 20.5
Buoyancy Flux (K m s^-1)				0.190
w*				1.04
tm (sec)				172
3 tm(sec)				518
Homogenous PBL Distance (m)				933

Table 9; Summary of data used for emissions estimate for May 17 2017 Run 1.

May 17 2017 - Run 1 (SB - east of KVL)	T1	T2	T3	Emission Estimate
Distance from KVL (m)	3080	5030	7305	
Integral (ppm*m)	222±9	67±9	49±15	49
Width of Plume (m)	2649	3614	6004	
Wind Speed (m/s)	3.8±0.2	7.1±0.4	7.1±2.2	6 ± 0.9
Wind Direction	251±24	210±0.5	208±19	223 ± 19.8
Theta				226
Cos Theta				0.69
PBL Height (m)				1277 ± 68
Pressure (Pa)	1009.4	1009.4	1009	1009.3 ± 0.2
Solar Intensity (watts / m^2)	752±52	792±8	727±218	757 ± 224
Buoyancy Flux (K m s^-1)				0.622
w*				2.96
tm (sec)				430
3 tm(sec)				1290
Homogenous PBL Distance (m)				9163

Table 10; Summary of data used for emissions estimate for May 17 2017 Run 2.

May 17 2017 - Run 2 (SB - east of KVL)	T1	T2	T3	Emission Estimate
Distance from KVL (m)	3080	5030	7305	
Integral (ppm*m)	226±2	90±15	49±15	49
Width of Plume (m)	2483	4091	4997	
Wind Speed (m/s)	6.8±1.3	5.6±0.7	5.1±1.1	5.8 ± 1.8
Wind Direction	222±11	256±30	212±13	230 ± 34
Theta				251
Cos Theta				0.325568
PBL Height (m)				1277 ± 68
Pressure (Pa)	1009	1009	1008.7	1008.9 ± 0.1
Solar Intensity (watts / m^2)	611±41	709±263	743±158	687.7 ± 309
Buoyancy Flux (K m s^-1)				0.565
w*				2.87
tm (sec)				444
3 tm(sec)				1332
Homogenous PBL Distance (m)				6796

Table 11. Summary of Emission Estimates of CH_4 from the KVL. * The data from May 16 2017 was not used in the overall emission estimate due to uncertainty with the PBL as discussed in greater detail in section 3.6

Date	Emission Estimate (kg / hr)
April 26 2017 - Run 1 (NB - West of KVL)	423 ± 73
April 26 2017 - Run 2 (NB - West of KVL)	187 ± 56
April 27 2017 - Run 2 (EB)	520 ± 106
May 16 2017 - Run 1 (EB) *	42 ± 5
May 17 2017 - Run 1 (SB - east of KVL)	749 ± 103
May 17 2017 - Run 2 (SB - east of KVL)	267 ± 97
Overall Emission Estimate	429 ± 199
Emission Inventory (2015)	2149.20

3.6 Discussion of Emission Estimates and Comparison with Inventory

The initial goal of this project was to calculate CH_4 emission estimates for multiple days with an expectation that the emission estimates would remain constant, within error, barring noise and uncertainties between each of the days. A number of factors lead to this not being the case with what

was observed from the field study (Figure 23). There was expected to be a trend of decreasing CH_4 integral from each transect as distance away from the KVL increased. This would have led to a levelling off of CH_4 levels, at a sufficiently far enough distance from the KVL, leading to easy identification of which integral to use when calculating the emission estimate. Due to the low number of transects driven a clear trend was not revealed and a theoretical distance of a homogeneously mixed boundary later,$3t_m$, was also calculated (Stull 1991 and Weil et al 2004).

The runs on April 26 2017 had a theoretical distance away from the KVL that fell between the distances of the first and second transects. April 27 2017 and May 16 2017 had a $3t_m$ that was closer than the distance to the nearest transect while May 17 2017 had a calculated $3t_m$ distance further than all three measured transects. All days are summarized in Figures 25 – 30. As shown in Figure 31 the emission estimates had significant variability from run to run. The April 27 and May 17 runs were carried out on days with highly variable wind which resulted in their emission estimates having the largest uncertainties associated with them. There was also a significant difference in emission estimates calculated on the same day for both April 26 and May 17. The integrals from the transects used on the same days were very similar as were the PBL's making the only significant difference in input to the calculation being the wind speed and wind direction. On both days a significant change in wind speed and direction was detected between the first and second runs. This makes this emission estimate method highly sensitive to both wind direction and PBL heights in determining final values and emphasizes the need to retrieve accurate values with consistent wind data for making final calculations.

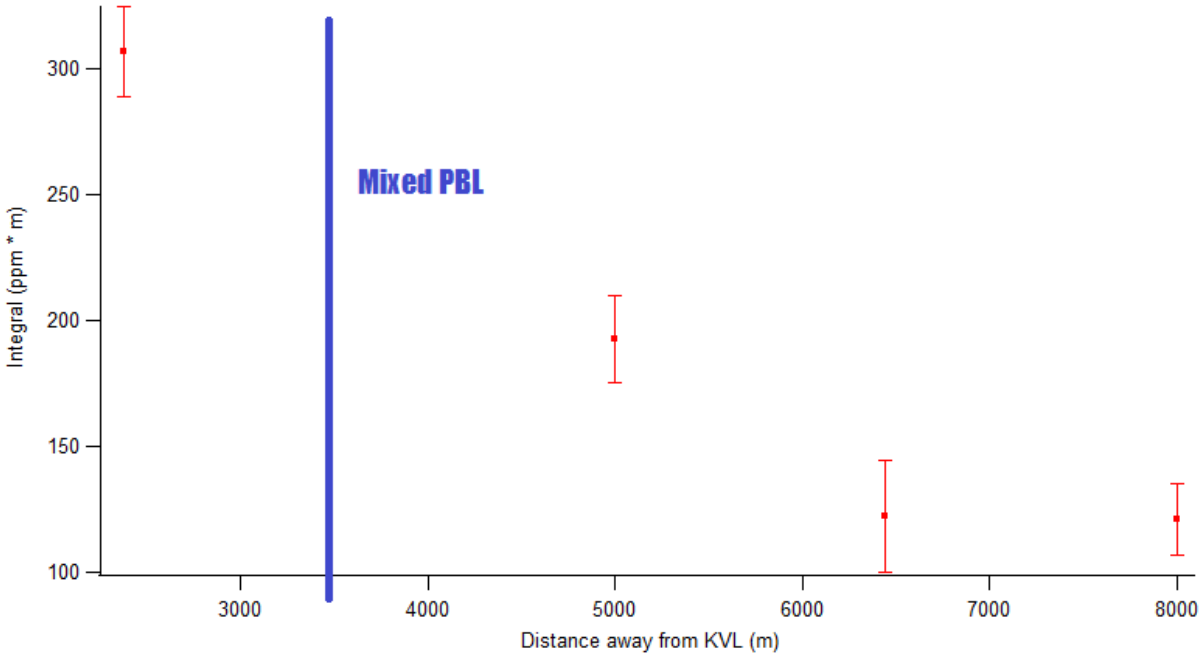

Figure 25; April 26 2017 - Run 1 Distance from the KVL and integral of CH_4 concertation. The blue line is the calculated theoretical distance for a homogeneously mixed PBL for this day's meteorological conditions.

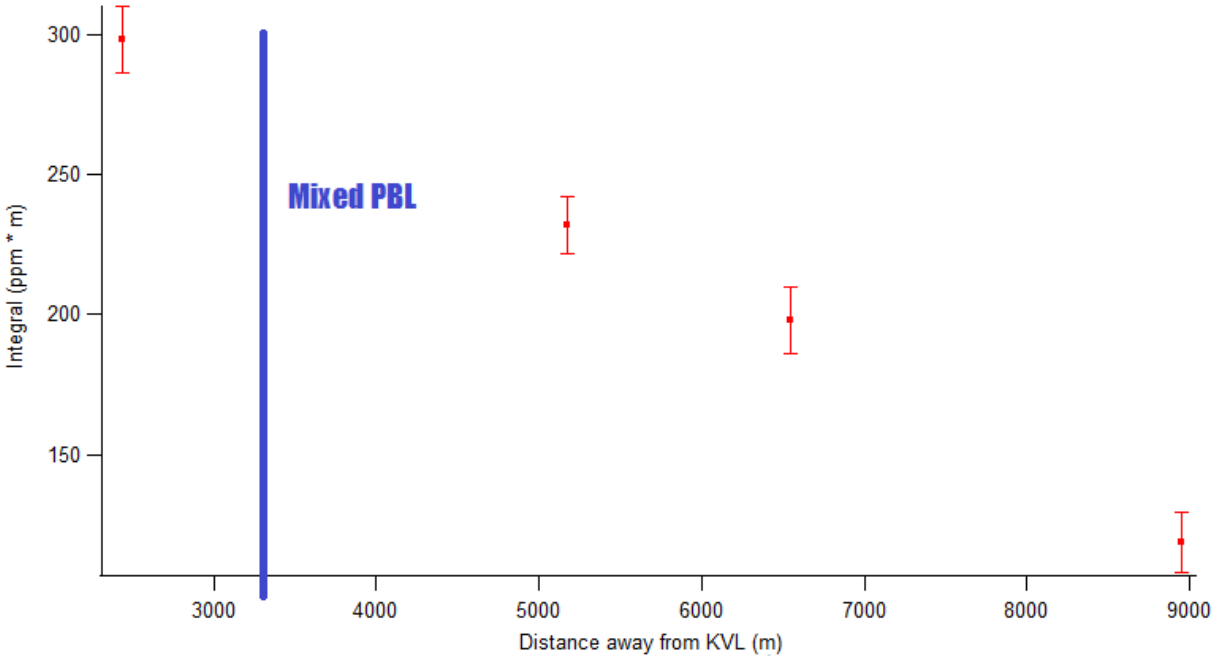

Figure 136; April 26 2017 - Run 2 Distance from the KVL and integral of CH_4 concertation. The blue line is the calculated theoretical distance for a homogeneously mixed PBL for this day's meteorological conditions.

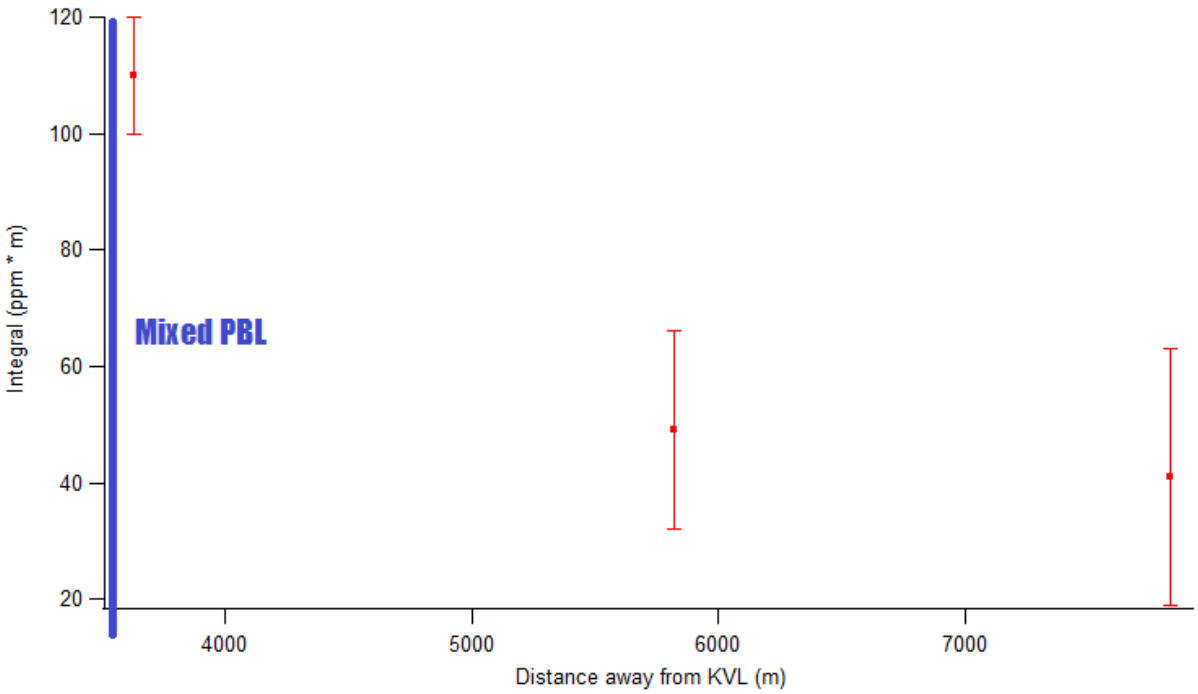

Figure 27; April 27 2017 - Run 2 Distance from the KVL and integral of CH_4 concertation. The blue line is the calculated theoretical distance for a homogeneously mixed PBL for this day's meteorological conditions.

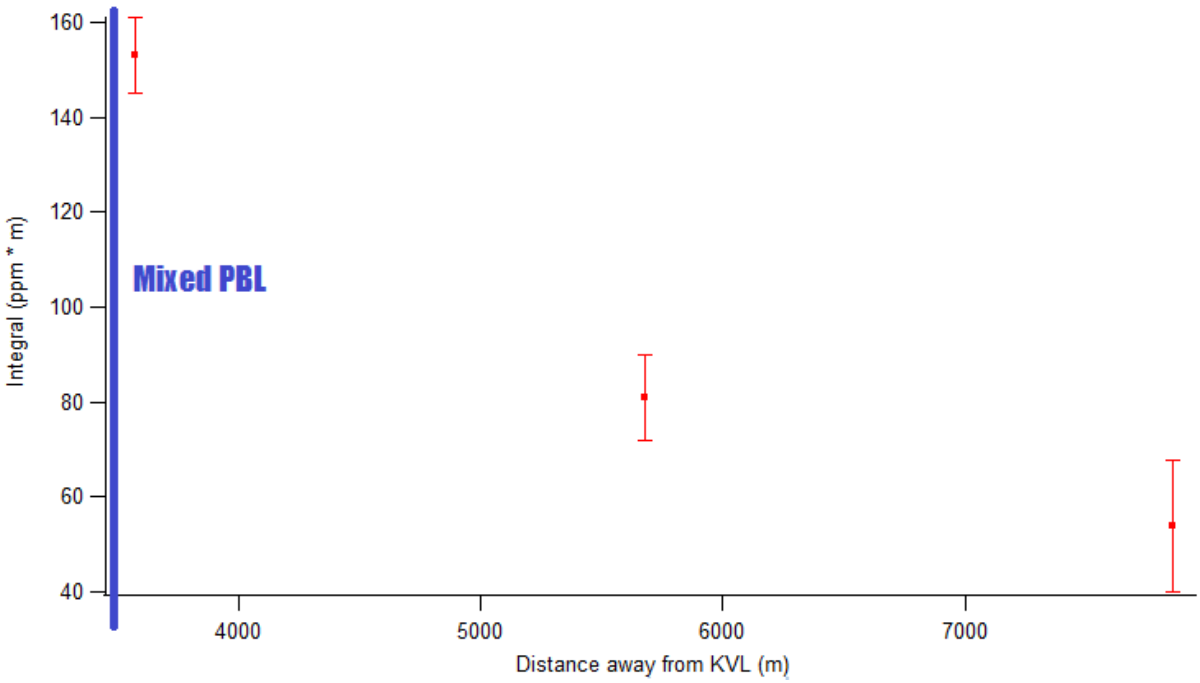

Figure 28; May 16 2017 - Run 1 Distance from the KVL and integral of CH_4 concertation. The blue line is the calculated theoretical distance for a homogeneously mixed PBL for this day's meteorological conditions.

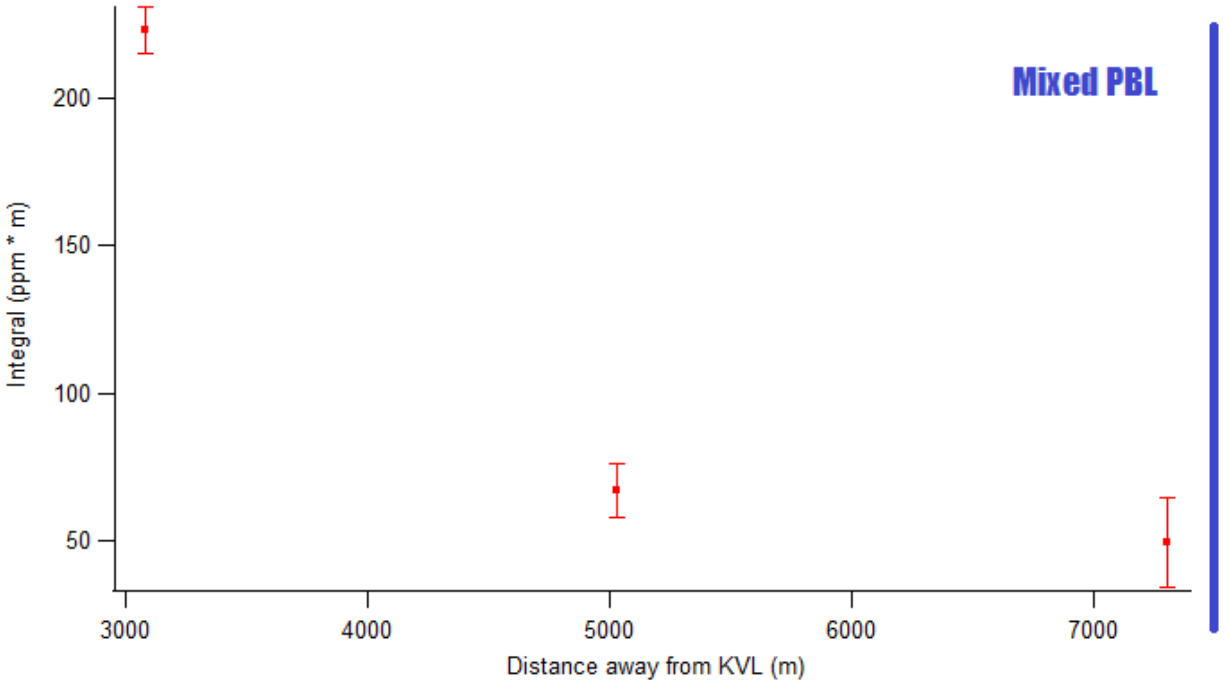

Figure 29; May 17 2017 - Run 1 Distance from the KVL and integral of CH_4 concertation. The blue line is the calculated theoretical distance for a homogeneously mixed PBL for this day's meteorological conditions.

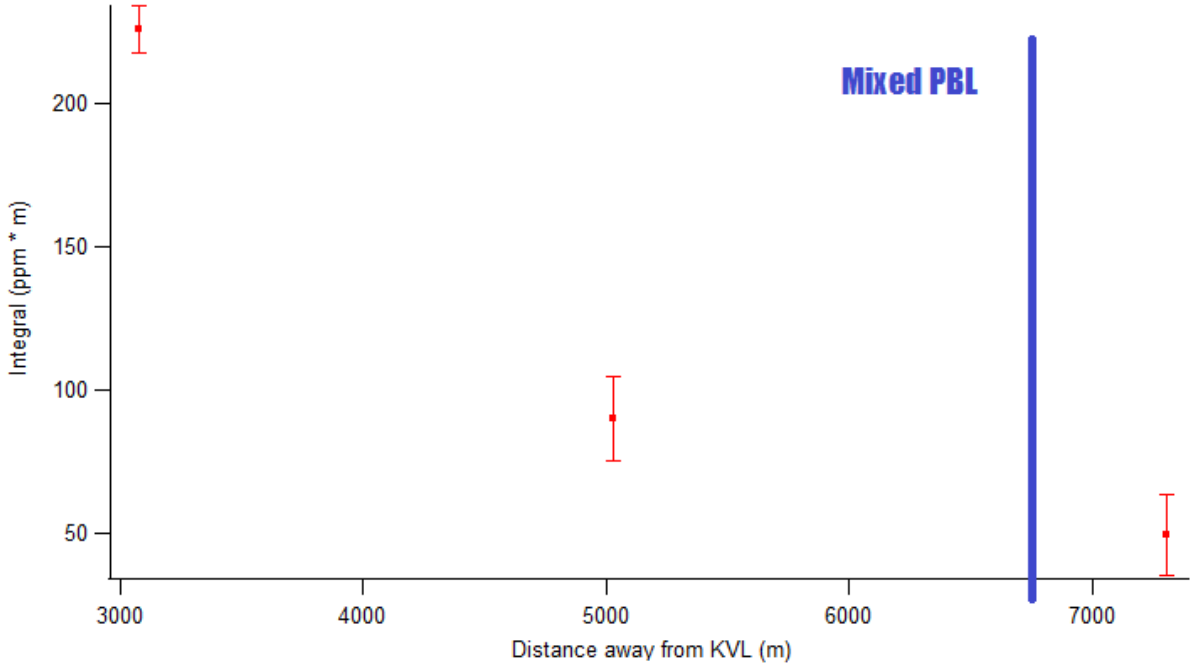

Figure 30; May 17 2017 - Run 2 Distance from the KVL and integral of CH_4 concertation. The blue line is the calculated theoretical distance for a homogeneously mixed PBL for this day's meteorological conditions.

This project also had the goal of using the TDL to make the measurements necessary for calculating the emission estimate. After the preliminary driving studies, in November 2016, it was shown that the CH_4 plume from the KVL was too wide to be fully captured by the TDL. At the time the longest path length, one way, successfully measured with the TDL was roughly 500m and the plume was nearly 2000m wide. This led to the idea of using the TDL at a location closer than the nearest driven transect to still give data on the trend of CH_4 mixing ratio during the field study but not to be used directly in any emission estimate calculations. The TDL was deployed on multiple days during the field study but proved challenging as the retro reflector was regularly knocked over on days with winds over 5 m/s. This resulted in only being able to include one day of viable CH_4 data from the TDL in this study.

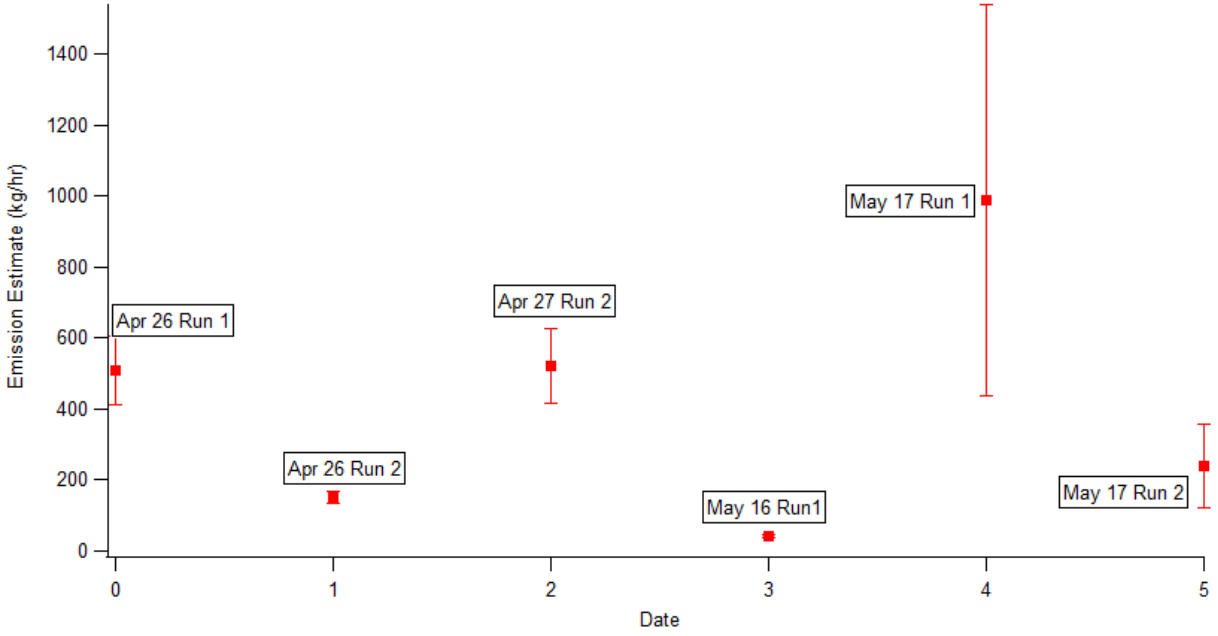

Figure 31; Emission Estimates for each run during the KVL field study

As seen in Figure 31 the large errors on the emission estimates from April 27 and May 17 2017 are due to the highly variable wind speed. Wind speeds were gusting during the day ranging from as low as 2-3 m/s up to over 8 m/s during the time it took from the first to last transect was driven. Previous studies have shown that variable wind speeds can result in inaccurate mass balance calculations as they have an underlying assumption of steady wind speed and direction (Karion et al 2013).

Emission Inventorys have been published for the KVL by Environment Canada since 2004, one year following the KVL's closure. The trend of emissions from year to year (Figure 32) does follow the theoretically expected trend given by the FOD method, with the exception of 2004 (Figure 7). The trend of increasing emissions is expected in the first 6 years where they will reach a maximum before decreasing at a rate of ten percent per year.

The average emission estimate calculated from the driving study was 429 ± 199 kg / hr. This value was significantly lower than the reported inventory value, from 2015, of 2149.20 kg / hr. The most sensitive variable input into the emission estimate calculation are the PBL heights. These values have the largest impact on changing the final emission value. This can be seen most easily by analyzing the data input for the May 16 emission estimate. The PBL data retrieved from the AMDAR database for May 16 had the PBL at a height of 180m whereas the other days of the field study had PBL's around the range of 1200m. This large discrepancy could have been caused due to the PBL heights on May 16 not being fully developed or being representative of the PBL at the KVL. If PBL heights were used on May 16 closer to those of the other days from the field study then the final emission estimate also come closer to average overserved value.

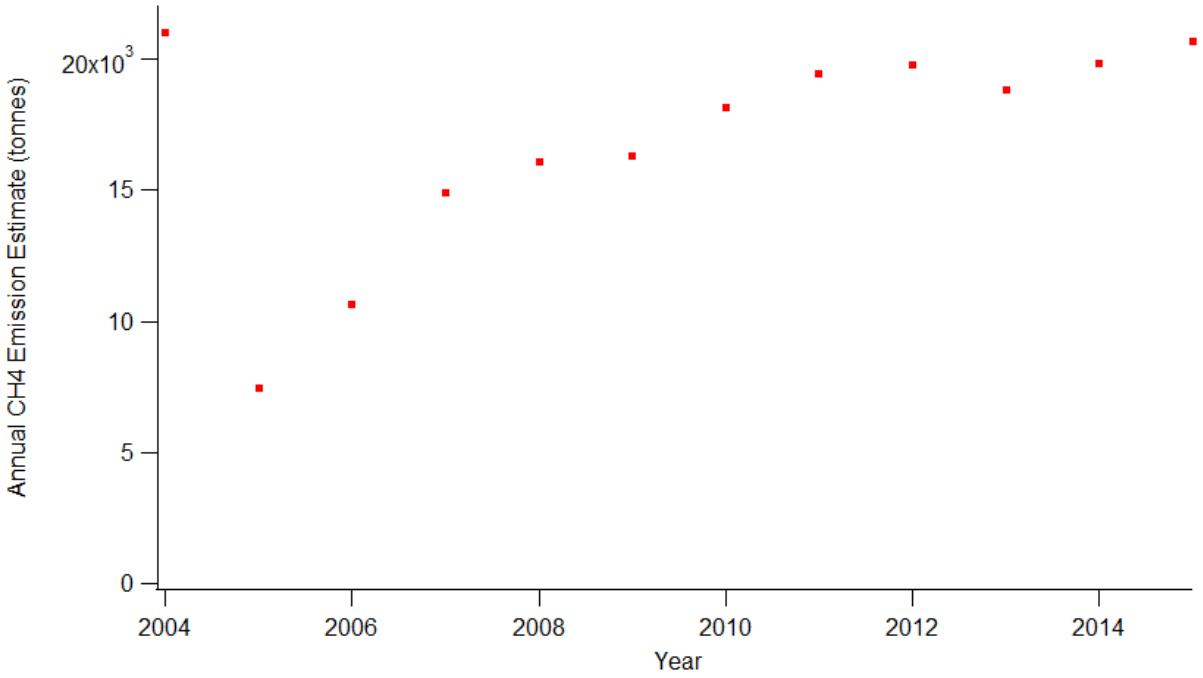

Figure 32; Reported CH_4 Inventory Emission rates from 2004 to 2015 as reported by Environment Canada.

Another factor that has been shown to influence landfill emissions is pressure (Czepiel et al 2003). This previous work has shown that emission rates at a US based landfill were negatively correlated with pressure. That trend was not clearly identified in the observations made at the KVL mainly due to the variable wind over the days of the experiments (Figure 33).

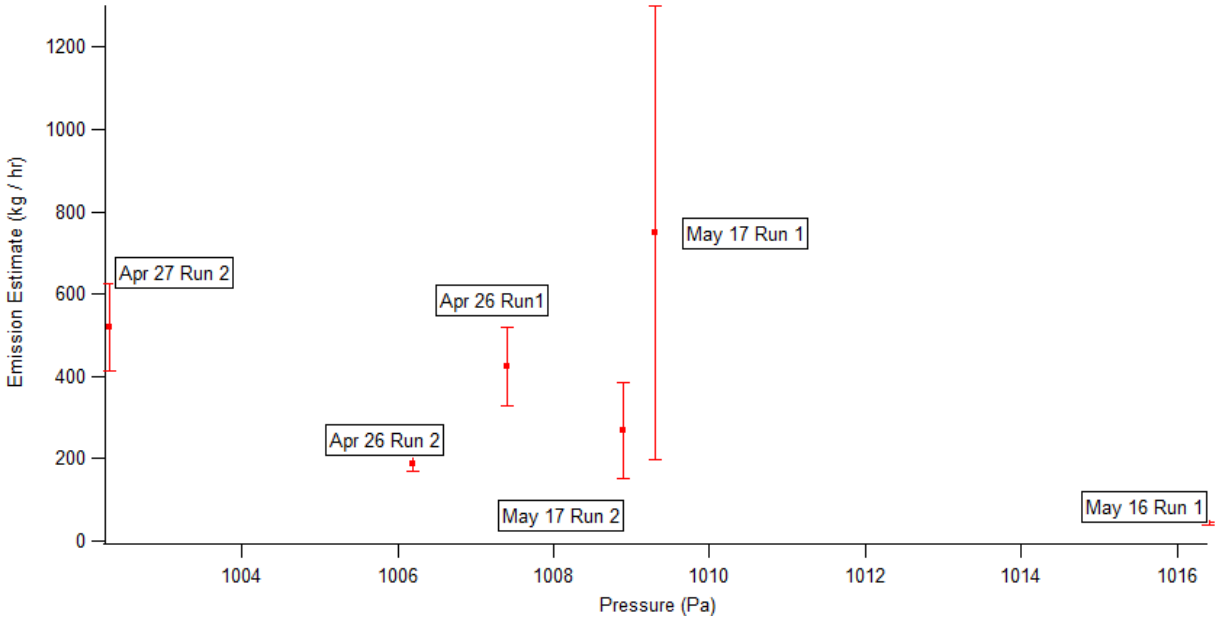

Figure 33; Plotting our Emission Estimate against atmospheric pressure for each run. The lack of expected negatively correlated mixing ratio with pressure is explained through the variable wind experienced on many of our days.

Meteorological studies looking into wind profiles at increasing heights have shown that wind speeds can vary greatly as height increases (Kikumoto et al, 2017). The underlying principle is based on the Power Law (PL) which is dependent on a reference height, z_n, wind speed at that height, U_n, and a Power Law Index (PLI), α.

$$U_{PL}(z) = U_n(\frac{z}{z_n})^{\alpha} \quad (28)$$

The PLI is based on the roughness of the ground level terrain (Architectural Institute of Japan, 2004). While the implications of these differences in wind speeds vertically from the ground to the height of the boundary layer may have made an impact on our emission estimates, they were not taken into account. The emissions estimates are calculated assuming that the furthest transect away is sufficient for a homogenous PBL regardless of these factors (Stull, 1991).

The power plant at the southern edge of the KVL was collecting underground CH_4 for the purpose of combustion and energy production which started during the landfill's construction (Keele Valley Gas to Energy Project, 2003). Close to the end of our study we were told by an employee of the plant that the gas is no longer being burned for energy production and is instead being flared. If this were the case then we would expect to see an enhancement of CO_2 and H_2O during peaks of CH_4 from the power plant.

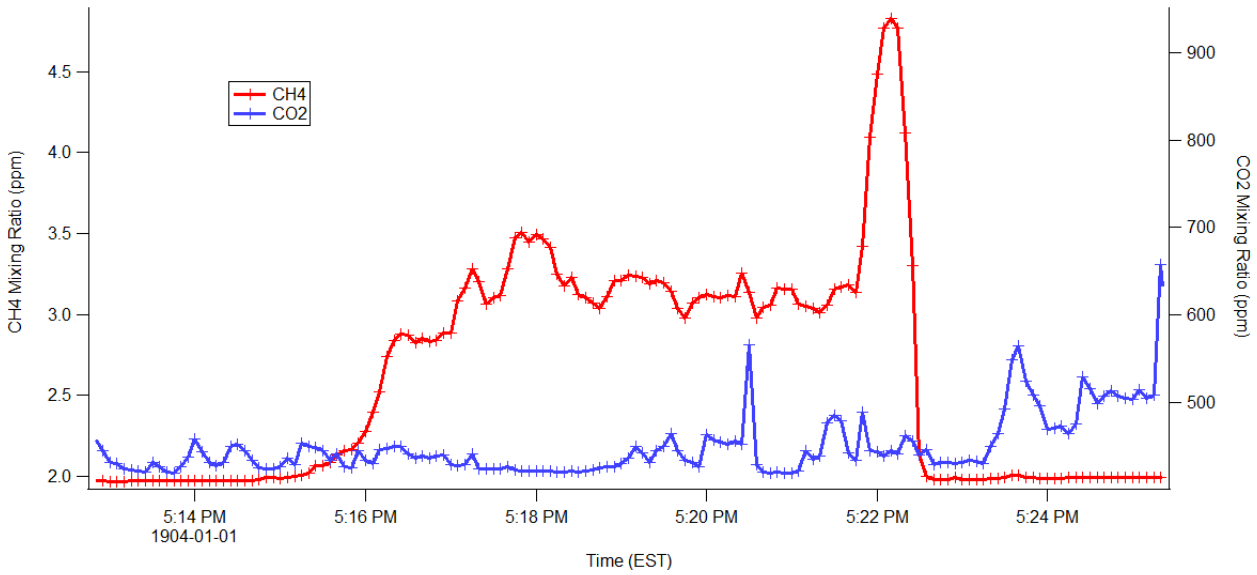

Figure 34; CH_4 and CO_2 mixing ratios from downwind of the KVL from Nov 29, 2016, at the time period during which the KVL power plant was supposedly flaring collected CH_4 gas.

If the power plant were flaring the CH_4 before release into the atmosphere, we would expect an enhancement of CO_2 and H_2O to be greater than that of the CH_4 enhancement observed. As shown in

Figure 34 there is was no significant enhancement of CO_2, above background levels, correlating with the observed CH_4 peak. This leads us to believe that the CH_4 was not being flared but still collected and then likely vented. This trend of a peak at the southern-most edge of the CH_4 enhancement was also duplicated during the later runs.

As seen below on April 28 2017 the enhancement of CH_4 passing the KVL downwind also occurs with a large peak at the southernmost edge before a plateau is detected but is not as clear as earlier measurement (Figure 34). A qualitative assessment of the CH_4 being released on the Nov 28 2016 run shows that a source at the southern end of the landfill, possibly in the vicinity of the power plant, is responsible for nearly 20% of the overall emissions. This was calculated by integrating the area underneath the southern peak and comparing it with the total area of the CH_4 enhancement. The peak from the April 28 run was more than 50% of the emission and was no longer clearly showing a distinct peak nor was it clearly at the southernmost edge of the enhancement. This could have been caused by the CH_4 capture no longer taking place and the CH_4 being left to seep out from the ground. When analyzing this data and the stark difference in our calculated emissions estimates with the emission inventory it leads us to believe that either the emission inventory is high or that the shutting off of the CH_4 capture and combustion system has somehow affected the rate at which CH_4 is being emitted by the KVL.

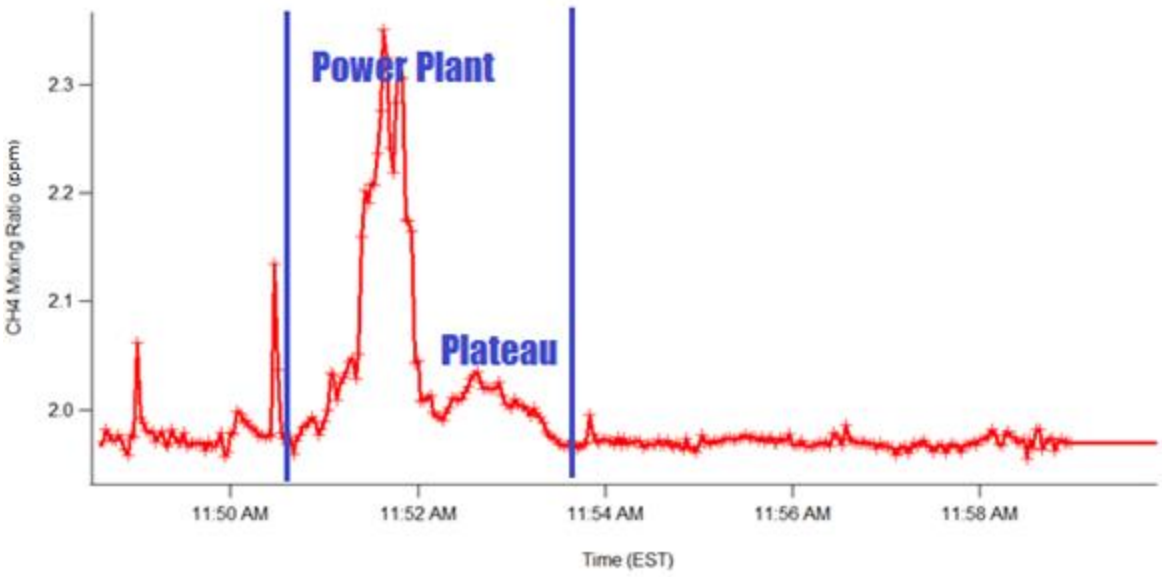

Figure 35; CH_4 enhancement downwind of the KVL from April 28 2017 drive northbound. The enhanced region of CH_4 begins with a peak from the Power Plant before detecting the ground releasing CH_4.

4.0 Future Work

This project has successfully presented a novel bottom-up ground-based method to quantify emissions and the work should be continued to be expanded upon. In particular the ground based method should be carried out in the future with a greater understanding of the PBL on each day of measurement. This can be done by a variety of methods most easily through LIDAR (Hennemuth and Lammert, 2006 and Menut et al 1999) or with a balloon sounding launch (Pagitz, 2007 and Cuxar et al, 2000). Both the LIDAR and balloon sounding options would be able to provide mobile cost-effective geographically relevant boundary layer information. This would reduce the uncertainty and need to use data from public sources that is either poorly correlated in time or geographically far away. Future projects could also be tested alongside aircraft studies which would allow for a direct comparison and validation of the method along with providing greater clarity on the overall emission of a given area.

Future studies following the same methodology should look at longer time frames as well as the impact of seasonality on CH_4 emissions. While all days should be considered, this work has shown that winds < 4 m/s and wind directions changing less than 30^o are ideal for producing the lowest errors associated with emission estimates. Days with highly variable gusting winds such as we presented here on May 17^{th} were shown to have the largest error and should be avoided for making a meaningful emission estimate.

References

AECOM Report (2017). Oak Ridges Air Management Facility Municipal Class Environmental Assessment Schedule B Project File

Anderson, D. Z., Frisch, J. C., & Masser, C. S. (1984). Mirror reflectometer based on optical cavity decay time. *Applied optics*, *23*(8), 1238-1245.

Architectural Institute of Japan, 2004. Recommendations for loads on buildings. Archit. Inst. Jpn.⟨http://www.aij.or.jp/jpn/symposium/2006/loads/loads.htm⟩

Bingemer, He G., and Paul J. Crutzen. "The production of methane from solid wastes." *Journal of Geophysical Research: Atmospheres* 92.D2 (1987): 2181-2187.

Bogner, J., M. Meadows, and P. Czepiel. "Fluxes of methane between landfills and the atmosphere: natural and engineered controls." *Soil Use and Management* 13.s4 (1997): 268-277.

Bogner, Jean, et al. "Mitigation of global greenhouse gas emissions from waste: conclusions and strategies from the Intergovernmental Panel on Climate Change (IPCC) Fourth Assessment Report. Working Group III (Mitigation)." *Waste Management & Research* 26.1 (2008): 11-32.

Butler, J. F., Calawa, A. R., Phelan Jr, R. J., Harman, T. C., Strauss, A. J., & Rediker, R. H. (1964). PbTe diode laser. *Applied Physics Letters*, *5*(4), 75-77.

Chappellaz, J. JM Barnola D. Raynaud YS Korotkevich C. Lorius. *Ice-core record of atmospheric methane over the past*, *160*, 127-131.

Cicerone, R. J., J. D. Shetter, and C. C. Delwiche. "Seasonal variation of methane flux from a California rice paddy." *Journal of Geophysical Research: Oceans* 88.C15 (1983): 11022-11024.

Conrad, Ralf. "Soil microorganisms as controllers of atmospheric trace gases (H2, CO, CH4, OCS, N2O, and NO)." *Microbiological reviews* 60.4 (1996): 609-640.

Cuxart, J., C. Yagüe, G. Morales, E. Terradellas, J. Orbe, J. Calvo, A. Fernández et al. "Stable atmospheric boundary-layer experiment in Spain (SABLES 98): a report." *Boundary-layer meteorology* 96, no. 3 (2000): 337-370.

Czepiel, P. M., Mosher, B., Crill, P. M., & Harriss, R. C. (1996). Quantifying the effect of oxidation on landfill methane emissions. *Journal of geophysical research: Atmospheres*, *101*(D11), 16721-16729.

Czepiel, P. M., J. H. Shorter, B. Mosher, E. Allwine, J. B. McManus, R. C. Harriss, C. E. Kolb, and B. K. Lamb. "The influence of atmospheric pressure on landfill methane emissions." *Waste Management* 23, no. 7 (2003): 593-598.

Dlugokencky, E. NOAA/ESRL (www.esrl.noaa.gov/gmd/ccgg/trends_ch4/)

Eng, R. S., Butler, J. F., & Linden, K. J. (1980). Tunable diode laser spectroscopy- An invited review. *Optical Engineering*, *19*(6), 945-960.

Fleming, I. R., R. K. Rowe, and D. Roy Cullimore. "Field observations of clogging in a landfill leachate collection system." *Canadian Geotechnical Journal* 36.4 (1999): 685-707.

Galle, B., Samuelsson, J., Svensson, B. H., & Börjesson, G. (2001). Measurements of methane emissions from landfills using a time correlation tracer method based on FTIR absorption spectroscopy. *Environmental Science & Technology*, *35*(1), 21-25.

Goulden, Michael L., et al. "Measurements of carbon sequestration by long-term eddy covariance: Methods and a critical evaluation of accuracy." *Global change biology* 2.3 (1996): 169-182.

Grimmond, C. S. B., et al. "Local-scale fluxes of carbon dioxide in urban environments: methodological challenges and results from Chicago." *Environmental Pollution* 116 (2002): S243-S254.

Harris, D. C. (2007). *Quantitative chemical analysis*. New York, NY: W.H. Freeman and Co.

Hedley, C. B., Saggar, S., & Tate, K. R. (2006). Procedure for fast simultaneous analysis of the greenhouse gases: methane, carbon dioxide, and nitrous oxide in air samples. *Communications in Soil Science and Plant Analysis*, *37*(11-12), 1501-1510.

Heemann, R., Laroque, D. O., Lourega, R. V., Rodrigues, L. F., Ketzer, J. M. M., & Goudinho, F. S. (2014). An Alternative Gas Chromatography Setting for Geochemical Analysis. *Journal of Chemical Engineering & Process Technology*.

Herndon, S. C., C. Daube, D. Jervis, T. I. Yacovitch, J. R. Roscioli, J. Curry, D. D. Nelson, and W. B. Knighton. "Quantification of emissions due to the natural gas storage well-casing blowout at Aliso Canyon/SS-25 using tracer flux ratio methods." In *AGU Fall Meeting Abstracts*. 2016.

Hennemuth, Barbara, and Andrea Lammert. "Determination of the atmospheric boundary layer height from radiosonde and lidar backscatter." *Boundary-Layer Meteorology* 120.1 (2006): 181-200.

IPCC, 2014: Climate Change 2014: Synthesis Report. Contribution of Working Groups I, II and III to the Fifth Assessment Report of the Intergovernmental Panel on Climate Change [Core Writing Team, R.K. Pachauri and L.A. Meyer (eds.)]. IPCC, Geneva, Switzerland, 151 pp.

"Keele Valley Gas to Energy Project". Environment Canada.
*h*ttps://web.archive.org/web/20031209203614/http://www.ec.gc.ca/nopp/lfg/en/issue4.cfm

Koga, R., Kosaka, M., & Sano, H. (1985). Field methane tracking with a portable and real-time open-gas monitor based on a cw-driven Pb-salt diode laser. *Optics & Laser Technology*, *17*(3), 139-144.

Kumar, Sunil, et al. "Estimation method for national methane emission from solid waste landfills." *Atmospheric Environment* 38.21 (2004): 3481-3487.

Lackner, M. (2007). Tunable diode laser absorption spectroscopy (TDLAS) in the process industries–a review. *Reviews in Chemical Engineering*, *23*(2), 65-147.

Menut, Laurent, Cyrille Flamant, Jacques Pelon, and Pierre H. Flamant. "Urban boundary-layer height determination from lidar measurements over the Paris area." *Applied Optics* 38, no. 6 (1999): 945-954.

Mohebati, A., & King, T. A. (1988). Remote detection of gases by diode laser spectroscopy. *Journal of modern optics*, *35*(3), 319-324.

Moore, C. B. (1965). Gas-laser frequency selection by molecular absorption. *Applied Optics*, *4*(2), 252-253.

Moriizumi, Jun, et al. "Carbon isotopic analysis of atmospheric methane in urban and suburban areas: fossil and non-fossil methane from local sources." *Atmospheric Environment* 32.17 (1998): 2947-2955.

Moriwaki, R., and M. Kanda. "Seasonal and diurnal fluxes of radiation, heat, water vapor, and carbon dioxide over a suburban area." *Journal of Applied Meteorology* 43.11 (2004): 1700-1710.

Oke, T. R. (1987). *Boundary layer climates*. London: Methuen.

Pagitz, Markus. "The future of scientific ballooning." *Philosophical Transactions of the Royal Society of London A: Mathematical, Physical and Engineering Sciences* 365.1861 (2007): 3003-3017.

Pétron, Gabrielle, Gregory Frost, Benjamin R. Miller, Adam I. Hirsch, Stephen A. Montzka, Anna Karion, Michael Trainer et al. "Hydrocarbon emissions characterization in the Colorado Front Range: A pilot study." *Journal of Geophysical Research: Atmospheres* 117, no. D4 (2012).

Potosnak, Mark J., et al. "Influence of biotic exchange and combustion sources on atmospheric CO2 concentrations in New England from observations at a forest flux tower." *Journal of Geophysical Research: Atmospheres* 104.D8 (1999): 9561-9569.

Quay, Paul, et al. "The isotopic composition of atmospheric methane." *Global Biogeochemical Cycles* 13.2 (1999): 445-461.

Rella, Chris W., Tracy R. Tsai, Connor G. Botkin, Eric R. Crosson, and David Steele. "Measuring emissions from oil and natural gas well pads using the mobile flux plane technique." *Environmental science & technology* 49, no. 7 (2015): 4742-4748.

Rigby, Matthew, Stephen A. Montzka, Ronald G. Prinn, James WC White, Dickon Young, Simon O'Doherty, Mark F. Lunt et al. "Role of atmospheric oxidation in recent methane growth." *Proceedings of the National Academy of Sciences* 114.21 (2017): 5373-5377.

Shemshad, J., Aminossadati, S. M., & Kizil, M. S. (2012). A review of developments in near infrared methane detection based on tunable diode laser. *Sensors and Actuators B: Chemical*, *171*, 77-92.

Soegaard, Henrik, and Lasse Møller-Jensen. "Towards a spatial CO 2 budget of a metropolitan region based on textural image classification and flux measurements." *Remote Sensing of Environment* 87.2 (2003): 283-294.

Stevens, Charles M., and Antoinette Engelkemeir. "Stable carbon isotopic composition of methane from some natural and anthropogenic sources." *Journal of Geophysical Research: Atmospheres* 93.D1 (1988): 725-733.

Turner, A. J., Frankenberg, C., Wennberg, P. O., and Jacob, D. J.: Ambiguity in the causes for decadal trends in atmospheric methane and hydroxyl, Proceedings of the National Academy of Sciences, 114, 5367-5372, 10.1073/pnas.1616020114, 2017.

Van Brummelen, Glen. *Heavenly Mathematics: The Forgotten Art of Spherical Trigonometry*. Princeton University Press, 2013. *JSTOR*, www.jstor.org/stable/j.ctt1r2fvb.

Velasco, Erik, et al. "Measurements of CO 2 fluxes from the Mexico City urban landscape." *Atmospheric Environment* 39.38 (2005): 7433-7446.

Walsh, Cindy J., et al. "Fluxes of atmospheric carbon dioxide over a suburban area of Vancouver." *Fifth Conference on Urban Environment*. 2004.

Warneck, Peter. *Chemistry of the Natural Atmosphere*. Vol. 41, Academic Press, 1988.